Research Square

Preprints are preliminary reports that have not undergone peer review.
They should not be considered conclusive, used to inform clinical practice,
or referenced by the media as validated information.

Integrated bulk and single-cell transcriptomic analysis identifies BCHE and FOXM1 as oxidative-stress markers linked to prognosis and immune-microenvironment remodeling in nasopharyngeal carcinoma

Zhao Chen
Second Affiliated Hospital of Dalian Medical University
Dan Wu
Second Affiliated Hospital of Dalian Medical University
Bo Sun
Second Affiliated Hospital of Dalian Medical University
Changyan Liu
Second Affiliated Hospital of Dalian Medical University
Mingli Zhao
Second Affiliated Hospital of Dalian Medical University
Yi Tian
Second Affiliated Hospital of Dalian Medical University
Xiaodan Kong
Second Affiliated Hospital of Dalian Medical University
Can Zhou
zhoucan1005@163.com

Second Affiliated Hospital of Dalian Medical University

Research Article

Keywords: nasopharyngeal carcinoma, oxidative stress, BCHE, FOXM1, prognosis, tumor immune microenvironment, single-cell RNA sequencing, bioinformatics

Posted Date: November 2nd, 2026

DOI: https://doi.org/10.21203/rs.3.rs-11297056/v1

License: This work is licensed under a Creative Commons Attribution 4.0 International License.
Read Full License

Additional Declarations: No competing interests reported.

Integrated bulk and single-cell transcriptomic analysis identifies BCHE and FOXM1 as oxidative-stress markers linked to prognosis and immune-microenvironment remodeling in nasopharyngeal carcinoma

Authors: Zhao Chen[1*], Dan Wu[1*], Bo Sun[1*], Changyan Liu[1], Mingli Zhao[1], Yi Tian[1,2], Xiaodan Kong[1,2], Can Zhou[1]

Author's department:[1] The Second Affiliated Hospital of Dalian Medical University; Dalian, China. [2]Key Laboratory of Autoantibody Detection of Dalian.

*Zhao Chen, Dan Wu and Bo Sun contributed equally to the work.

Corresponding author: Yi Tian and Xiaodan Kong, Department of Rheumatology, The Second Affiliated Hospital of Dalian Medical University; Key Laboratory of Autoantibody Detection of Dalian, Dalian, 116000, China, E-mail: 651183823@qq.com, Xiaodankong2008@sina.com; Can Zhou, MD, Department of Ear-Nose-Throat department, The Second Affiliated Hospital of Dalian Medical University, 467 Zhongshan Road, Dalian, 116000, China. E-mail: zhoucan1005@163.com;

Abstract

Background: Nasopharyngeal carcinoma (NPC), an Epstein–Barr virus–associated head-and-neck cancer, typically carries dense yet dysfunctional immune infiltrates. Oxidative stress shapes both tumor progression and immune escape; whether oxidative-stress genes (OSGs) carry prognostic and immunological information in NPC has not been examined at bulk and single-cell resolution. **Methods:** Three NPC microarray cohorts (GSE12452, GSE53819 and GSE64634) were integrated using robust rank aggregation and ComBat-corrected limma, and genes identified by both strategies were intersected with 1,398 OSGs from GeneCards. Candidate prognostic OSGs were tested in the RNA-seq cohort GSE102349 (n = 88) using univariate Cox, LASSO and multivariable Cox regression together with Kaplan–Meier analysis, time-dependent ROC curves and a nomogram. We further applied Hallmark gene-set enrichment, CIBERSORT, an immune-cell LASSO signature, checkpoint correlation, ssGSEA and drug-sensitivity prediction, and replicated the findings in three independent cohorts and a single-cell RNA-seq dataset

(GSE150430), where in-silico knockout, transcription-factor regulon, trajectory and cell–cell communication analyses were also performed. **Results:** Of 722 consistent differentially expressed genes, 67 were NPC-specific OSGs. BCHE emerged as the consistently prognostic OSG (univariate HR = 1.85, P = 0.009; optimal-cutoff Kaplan–Meier P = 0.003, high-versus-low HR = 4.1; the sole LASSO-retained multivariable term). FOXM1 failed multivariable retention but still defined a high-risk subgroup by optimal-cutoff Kaplan–Meier (P = 0.012, HR = 4.4). Enrichment analysis tied FOXM1 to E2F/G2M/MYC proliferation programs and BCHE to epithelial–mesenchymal-transition and Wnt signaling; both genes were inversely related to interferon and complement pathways. A ten-cell immune signature and checkpoint correlations outlined an immune-suppressed compartment. At single-cell level, both genes localized to malignant cells within a shared early malignant state, and malignant–immune crosstalk was dominated by MIF- and galectin-mediated signaling. **Conclusion:** Convergent bulk and single-cell evidence supports BCHE as a prognostic OS marker for risk stratification and FOXM1 as a proliferation-linked marker of malignant state in NPC. Both track with immune-microenvironment remodeling and await experimental and prospective validation.

Keywords: nasopharyngeal carcinoma; oxidative stress; BCHE; FOXM1; prognosis; tumor immune microenvironment; single-cell RNA sequencing; bioinformatics

1. Introduction

Nasopharyngeal carcinoma arises from the epithelial lining of the nasopharynx and shows one of the most skewed geographic distributions of any human cancer. It is uncommon outside East and Southeast Asia but reaches high incidence across southern China (1, 2). In endemic regions, more than 95% of tumors are undifferentiated non-keratinizing carcinomas, and virtually all of them harbor Epstein–Barr virus (EBV) (3). The tumor sits deep in the nasopharynx and produces few early symptoms, so most patients present with locoregionally advanced disease. Concurrent chemoradiotherapy gives excellent local control; failure, when it occurs, is usually distant metastasis or recurrence (4). Molecular markers that can sharpen prognosis and describe the tumor microenvironment (TME) remain in short supply.

Oxidative stress reflects a mismatch between reactive oxygen species (ROS) production and antioxidant capacity, and its role in cancer is context dependent (5). At intermediate concentrations, ROS promote proliferation, genomic instability, epithelial–mesenchymal transition (EMT) and treatment resistance, and they reshape the TME by altering leukocyte recruitment and functional state (6, 7). OS-related genes (OSGs) already serve as prognostic indicators in several tumor types. A systematic, multi-cohort analysis of OSGs in NPC, including how they relate to immune infiltration, is still missing.

Public transcriptomic repositories now offer enough independent NPC datasets for integrative, hypothesis-free screening. We combined three microarray cohorts using two complementary differential-expression strategies, robust rank aggregation (RRA) and ComBat-corrected limma, and intersected the shared genes with a curated OSG list. An independent RNA-seq survival cohort then identified BCHE as the OSG with the strongest prognostic evidence and FOXM1 as an OSG linked to proliferation. Both genes were further characterized by functional enrichment, GSEA, CIBERSORT and LASSO-based immune deconvolution, ssGSEA, checkpoint and drug-sensitivity analyses, with cross-cohort and single-cell validation (Figure 1). The result is a reproducible OS-centered workflow and two candidate biomarkers for NPC risk stratification.

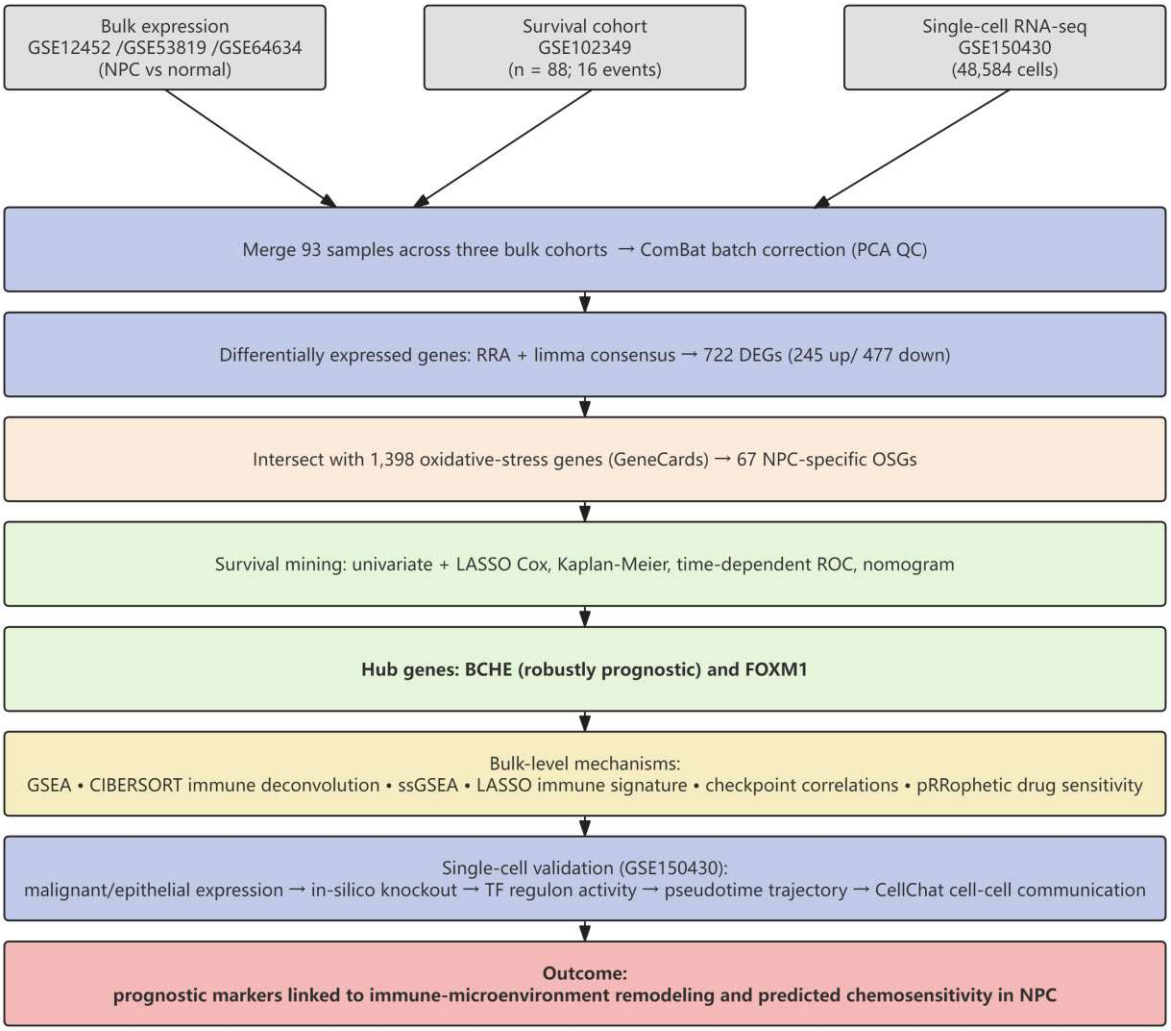


Figure 1. Study workflow. Three NPC microarray datasets were integrated by RRA and ComBat-corrected limma to obtain consistent DEGs, which were intersected with oxidative-stress genes. Prognostic OSGs were selected in GSE102349 and characterized by ROC/nomogram, GSEA, immune deconvolution, checkpoint/drug analysis, and validated across three independent NPC cohorts and by single-cell RNA-seq.

2. Materials and Methods

2.1 Data acquisition and study design

The workflow is outlined in Figure 1. Three NPC microarray datasets were obtained from the Gene Expression Omnibus (GEO, https://www.ncbi.nlm.nih.gov/geo/) (8): GSE12452 (GPL570; 31 NPC and 10 normal nasopharyngeal samples), GSE53819 (GPL6480; 18 NPC and 18 non-cancerous nasopharyngeal samples) and GSE64634 (GPL570; 12 NPC and 4 normal samples). GSE102349 (GPL11154), an RNA-seq cohort of 113 treatment-naïve undifferentiated NPC tumors, 88 with complete time-to-event

data, was used for prognostic modeling. GSE150430 provided single-cell validation. All analyses were conducted on human gene symbols; probe-level values were collapsed to genes by keeping the probe with the highest mean expression. Log-scale expression was confirmed before analysis.

2.2 Acquisition of oxidative stress-related genes

OSGs were downloaded from GeneCards (https://www.genecards.org) (9) with the query "oxidative stress". Genes with a relevance score of at least 7 were retained, giving 1,398 OSGs. NPC-specific OSGs were defined as the overlap between this set and the consistent differentially expressed genes.

2.3 DEG screening: RRA and ComBat-corrected limma

Within each dataset, differential expression between NPC and normal tissue was computed with limma (10), using an empirical Bayes moderated t-test. Two integration routes were then followed. First, gene lists ranked by t-statistic were combined by robust rank aggregation (RRA, RobustRankAggreg R package) (11) with false-discovery-rate (FDR) correction; genes with FDR $\leq$ 0.05 and |mean log2 fold-change (logFC)| > 1 formed the RRA list. Second, the three matrices were merged on shared genes and adjusted for dataset effects with ComBat (sva package) (12, 13) while the biological grouping was retained; limma was then re-run (adjusted P $\leq$ 0.05, |logFC| > 1). Genes detected by both routes were defined as consistent DEGs. Boxplots and principal component analysis (PCA), before and after ComBat, were used to verify batch removal.

2.4 Functional enrichment

Gene Ontology (GO; biological process, cellular component and molecular function) (14) and Kyoto Encyclopedia of Genes and Genomes (KEGG) (15) enrichment of consistent DEGs and NPC-specific OSGs was run in clusterProfiler (16). FDR $\leq$ 0.05 was considered significant.

2.5 Survival analysis and prognostic gene selection

In GSE102349, time to event in months and event status (disease progression = 1, last follow-up = 0) were extracted for 88 tumors with complete records. Each NPC-

specific OSG was first assessed by univariate Cox proportional-hazards regression. Given the small number of events, candidates with $P < 0.1$ entered a LASSO-Cox with ten-fold cross-validation (17) to limit overfitting, followed by multivariable Cox regression to identify independent prognostic genes. Kaplan–Meier curves with log-rank tests compared survival between high- and low-expression groups defined by the optimal cutoff (survminer::surv_cutpoint).

2.6 Time-dependent ROC, nomogram and calibration

Time-dependent receiver-operating characteristic (ROC) curves at 1 and 3 years were produced with timeROC (18); 5-year curves were not estimated because follow-up did not reach five years. A nomogram combining the retained prognostic genes, together with clinical stage where available, was built with the rms package (19). Discrimination was quantified by the concordance index (C-index) with 1,000-bootstrap internal validation, and calibration curves compared predicted with observed survival.

2.7 Gene set enrichment analysis

For each hub gene, samples were ranked by Spearman correlation between hub-gene expression and the whole transcriptome, and GSEA (20) against the Hallmark collection (MSigDB) (21) was run in clusterProfiler with 1,000 permutations. Gene sets with nominal $P < 0.05$ and FDR < 0.25 were treated as enriched.

2.8 Immune infiltration: CIBERSORT and LASSO

The fractions of 22 tumor-infiltrating leukocyte subsets were estimated by CIBERSORT (22) using the LM22 signature and 1,000 permutations; samples with CIBERSORT $P \geq 0.05$ were excluded. Differences between NPC and normal tissue were tested with the Wilcoxon rank-sum test, and correlations between subsets were plotted. LASSO logistic regression (10-fold cross-validation, binomial family) identified the most discriminative subsets; the overlap between LASSO-selected and significantly differential subsets defined the final immune signature.

2.9 Gene–immune and immune-checkpoint correlation; ssGSEA

Spearman correlation was used to relate FOXM1 and BCHE expression to the signature subsets and to a panel of checkpoint genes (PDCD1, CD274, CTLA4, LAG3, HAVCR2 and TIGIT, among others). Single-sample GSEA (ssGSEA), implemented through the GSVA package (23) with a curated 28-cell immune signature, provided an independent immune score.

2.10 Drug-sensitivity prediction

Drug sensitivity was predicted with pRRophetic (24), which estimates the half-maximal inhibitory concentration (IC50) by ridge regression against the Cancer Genome Project/Genomics of Drug Sensitivity in Cancer cell-line panel (25). Group comparisons used the Wilcoxon test.

2.11 External cohort and single-cell validation

External bulk validation used the three independent NPC microarray cohorts GSE12452, GSE53819 and GSE64634; FOXM1 and BCHE expression in NPC versus normal nasopharyngeal tissue was compared by Wilcoxon test. GSE150430 was processed with Seurat (26), including quality control, normalization, PCA, graph-based clustering and UMAP, using the authors' cell-type annotations. Hub-gene expression across cell types was summarized with FeaturePlot, DotPlot and VlnPlot, and malignant cells were compared directly with non-malignant epithelial cells by Wilcoxon test. The Human Protein Atlas pathology atlas does not cover nasopharyngeal carcinoma; its head-and-neck category is TCGA head-and-neck squamous cell carcinoma, a different disease. With no NPC-specific immunohistochemistry available, we make no protein-level claim and rely instead on concordant bulk cohorts and cell-resolved single-cell data.

2.12 Single-cell perturbation, trajectory and cell–cell communication

In-silico knockout of FOXM1 and BCHE in malignant cells was performed with scTenifoldKnk (27), which builds ten bootstrap gene-regulatory networks for wild-type and virtual-knockout states and aligns the resulting manifolds; log-normalized expression was first back-transformed to a linear scale. Co-expression modules were defined by Spearman correlation and tested by GO enrichment. Transcription-factor regulon activity was scored per cell using DoRothEA regulons (confidence A–C) and the viper algorithm

(28), as a SCENIC-style analysis (29). Malignant-cell trajectories were inferred with monocle3 (30) and verified with slingshot. CellChat (31) was used to infer intercellular communication in the NPC microenvironment (each population capped at 400 cells; 100 permutations), with ligand–receptor and pathway-level probabilities quantified separately for outgoing and incoming signaling.

2.13 Statistical analysis

All analyses were performed in R v4.6.1 (R Foundation for Statistical Computing). Tests were two-sided, and $P < 0.05$ was considered significant unless stated otherwise. The Benjamini–Hochberg procedure controlled the FDR. Plots were generated with ggplot2 (32), pheatmap and survminer.

3. Results

3.1 Identification of consistent DEGs across three NPC cohorts

After probe-to-gene collapse and log-scale checks, the three datasets contained matched NPC and normal samples (GSE12452, 31 versus 10; GSE53819, 18 versus 18; GSE64634, 12 versus 4). Aggregating per-dataset limma statistics by RRA yielded 866 DEGs (FDR ≤ 0.05, $|\text{mean logFC}| > 1$). Merging the matrices on common genes and applying ComBat removed dataset clustering: samples grouped by dataset before correction and intermingled afterward, while NPC and normal samples remained separated (Figure S1A–D). Limma on the corrected matrix produced 972 DEGs. The two lists overlapped in 722 consistent DEGs (Figure 2C), which fed all downstream analyses. Heatmaps of the highest-ranked RRA and limma DEGs showed coherent NPC-versus-normal clustering (Figure 2A,B).

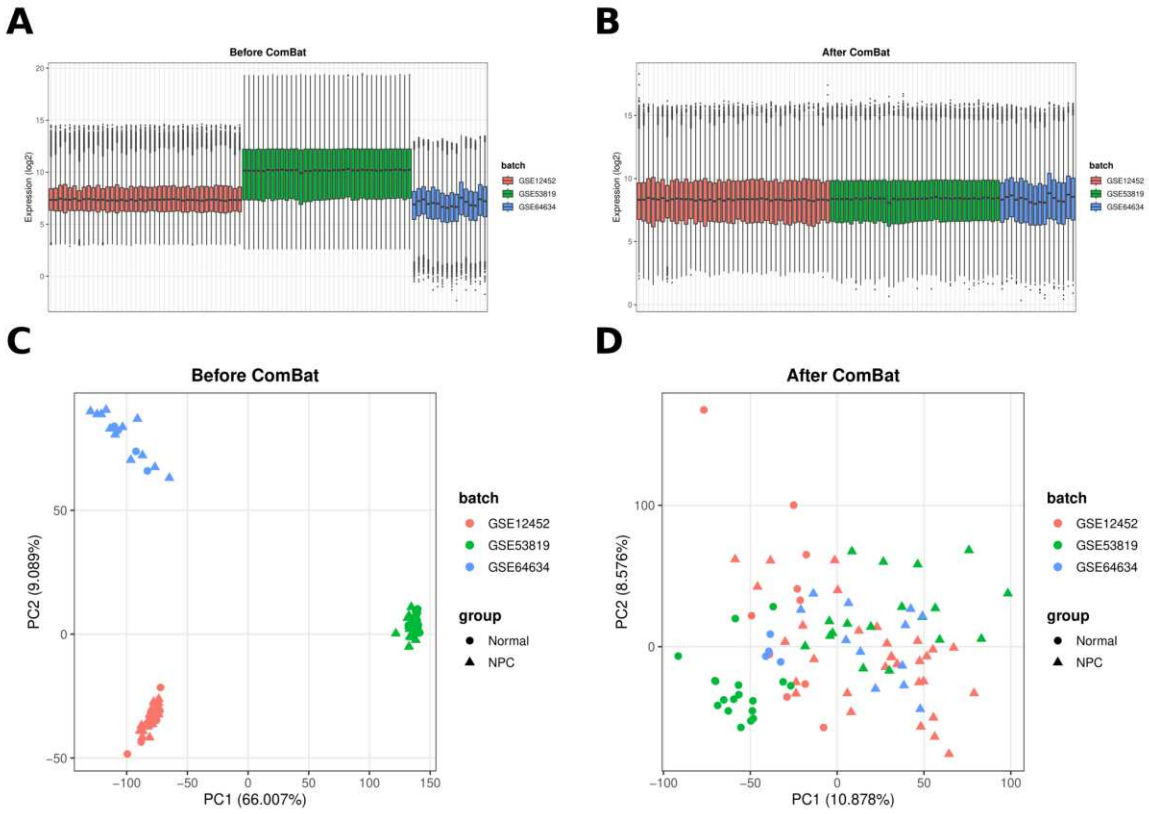


Figure S1. Batch-correction QC. Boxplots (A, B) and PCA (C, D) before and after ComBat.

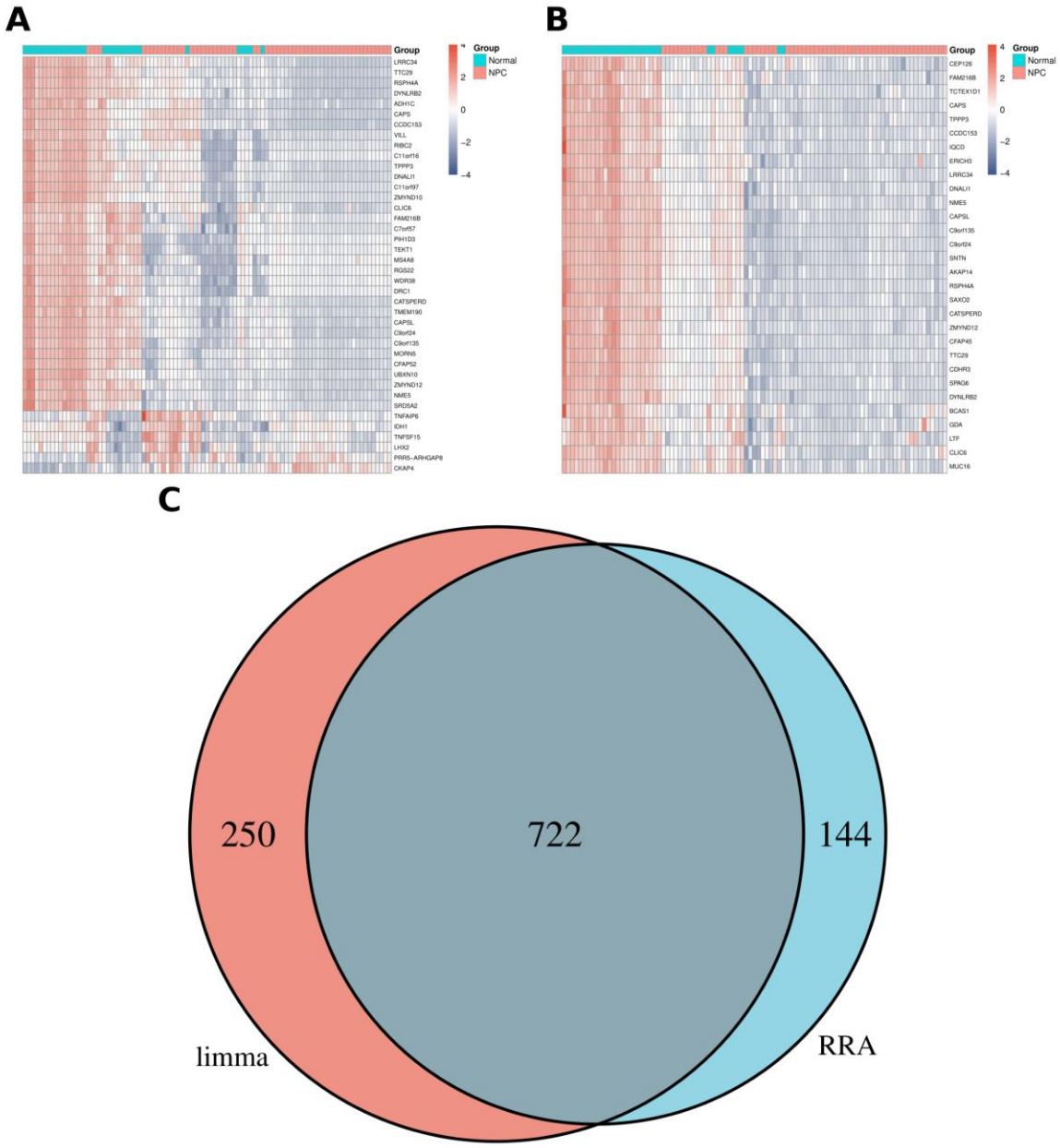


Figure 2. Identification of consistent DEGs. (A) Heatmap of the top 40 RRA DEGs; (B) heatmap of the top 30 batch-corrected limma DEGs; (C) Venn diagram of the 866 RRA and 972 limma DEG lists (intersection = 722).

3.2 Functional profile of the consistent DEGs

GO analysis of the 722 DEGs was dominated by motile-cilium and microtubule programs. Cilium movement led the biological-process terms (adjusted P = 7.4×10^{-31}), followed by microtubule-based movement and cilium-dependent motility; axoneme and ciliary plasm headed cellular-component terms (adjusted P ≈ 1.2×10^{-28}); and microtubule motor activity, tubulin binding and extracellular-matrix structural

constituents led molecular function (all adjusted $P < 1 \times 10^{-6}$; Figure 3A). KEGG analysis highlighted amoebiasis (adjusted $P = 3.9 \times 10^{-5}$), complement and coagulation cascades, motor proteins, protein digestion and absorption, and cytokine–cytokine-receptor interaction (all adjusted $P < 0.05$; Figure 3B). The combined picture is loss of epithelial ciliary architecture, ECM and structural remodeling, and complement-driven inflammatory signaling in NPC.

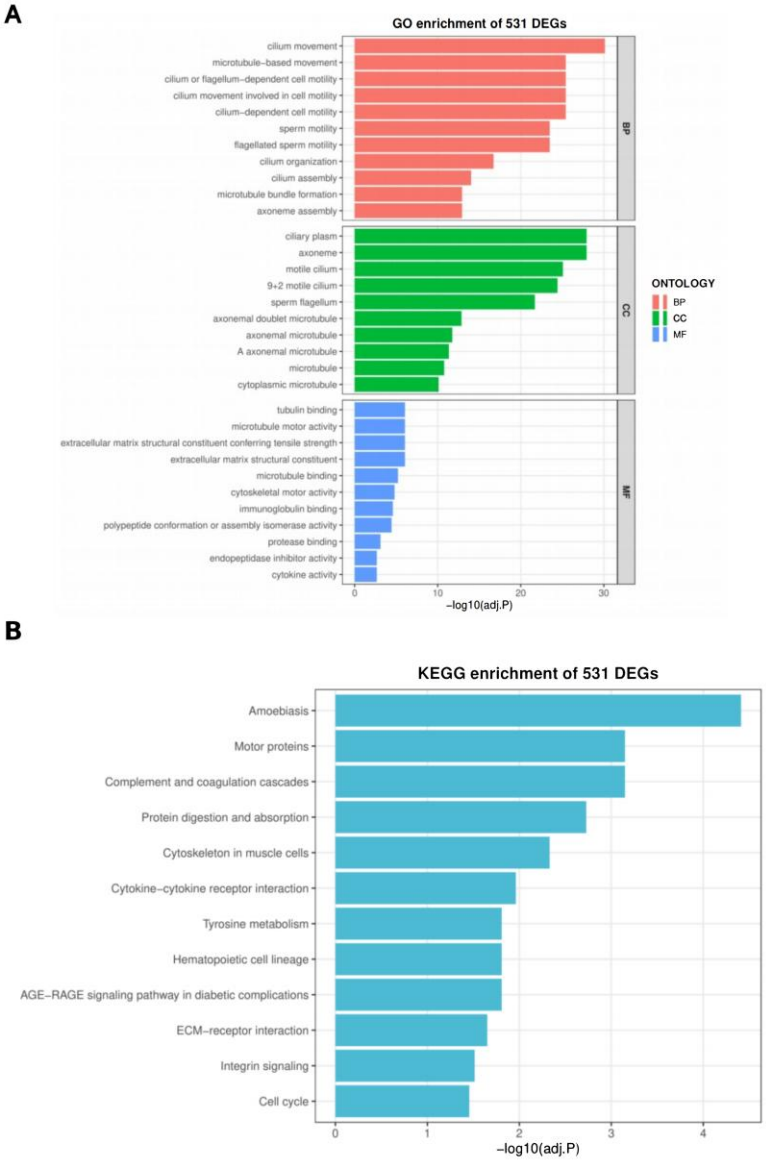


Figure 3. Enrichment of the 722 consistent DEGs. (A) GO (BP/CC/MF) bar plot, led by cilium and microtubule-movement biological-process terms, axoneme/ciliary-plasm cellular components and extracellular-matrix structural constituents; (B) KEGG dot/bar plot (amoebiasis, complement and coagulation cascades, motor proteins and cytokine–cytokine-receptor interaction).

3.3 Sixty-seven OS-related DEGs and their enrichment

Intersecting the 1,398 GeneCards OSGs with the 722 consistent DEGs gave 67 NPC-specific OSGs, 36 up-regulated and 31 down-regulated (Figure 4A). Their expression cleanly separated NPC from normal tissue (Figure 4B), and the volcano plot confirmed the mixed direction of change (Figure 4C). The set was not limited to antioxidant enzymes. GO enrichment highlighted humoral immune response (adjusted P = 7.9×10^{-8}), negative regulation of immune effector processes and response to lipopolysaccharide and bacterial stimuli (biological process); secretory granule and vesicle lumen (cellular component); and cytokine activity with cytokine-receptor binding (molecular function, adjusted P = 4.0×10^{-6}) (Figure 5A). KEGG enrichment identified complement and coagulation cascades (adjusted P = 1.3×10^{-5}), the IL-17, NF-κB and HIF-1 pathways, and cytokine–cytokine-receptor interaction (Figure 5B), placing oxidative stress within the inflammatory, hypoxic and cytokine signaling of the NPC microenvironment.

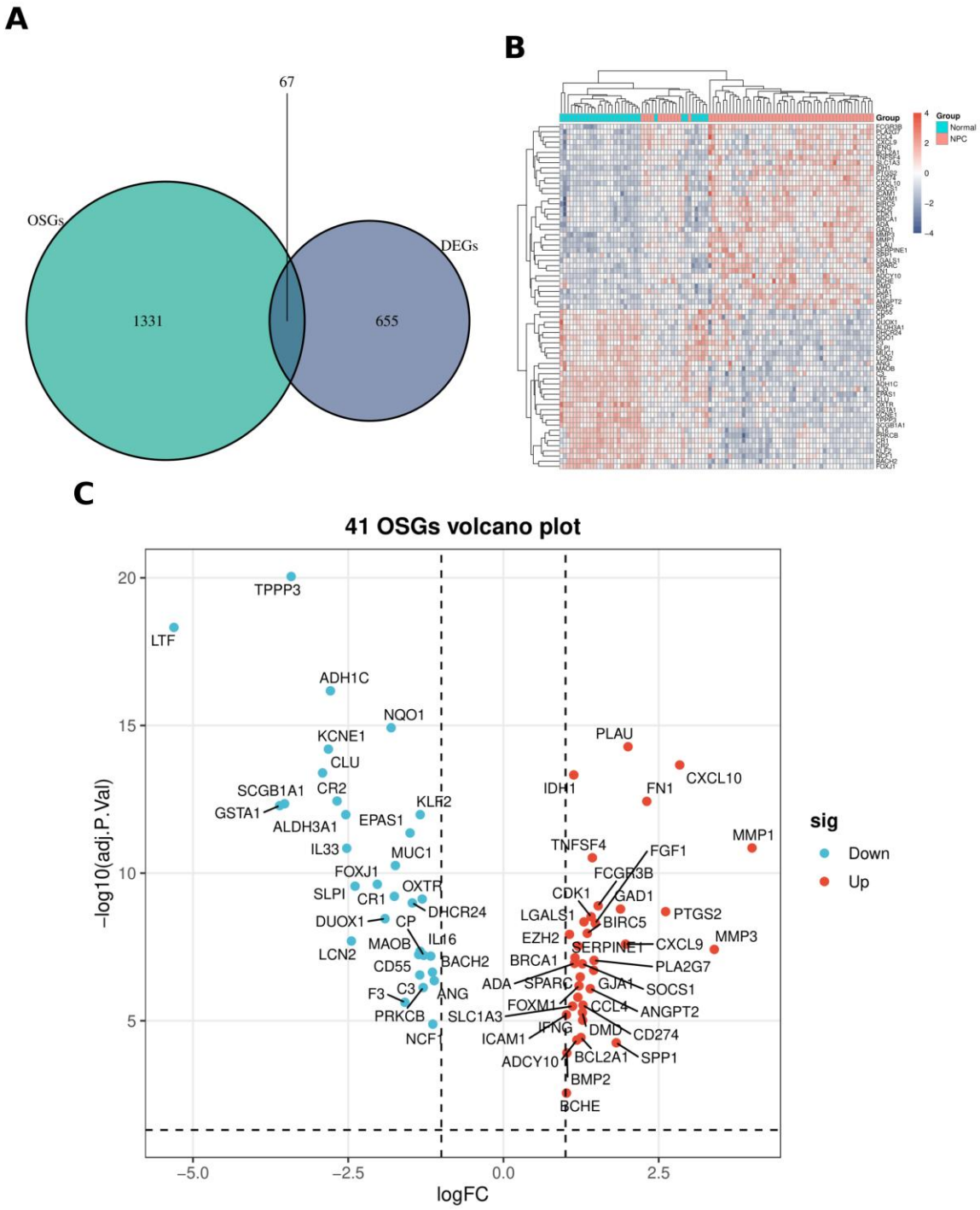
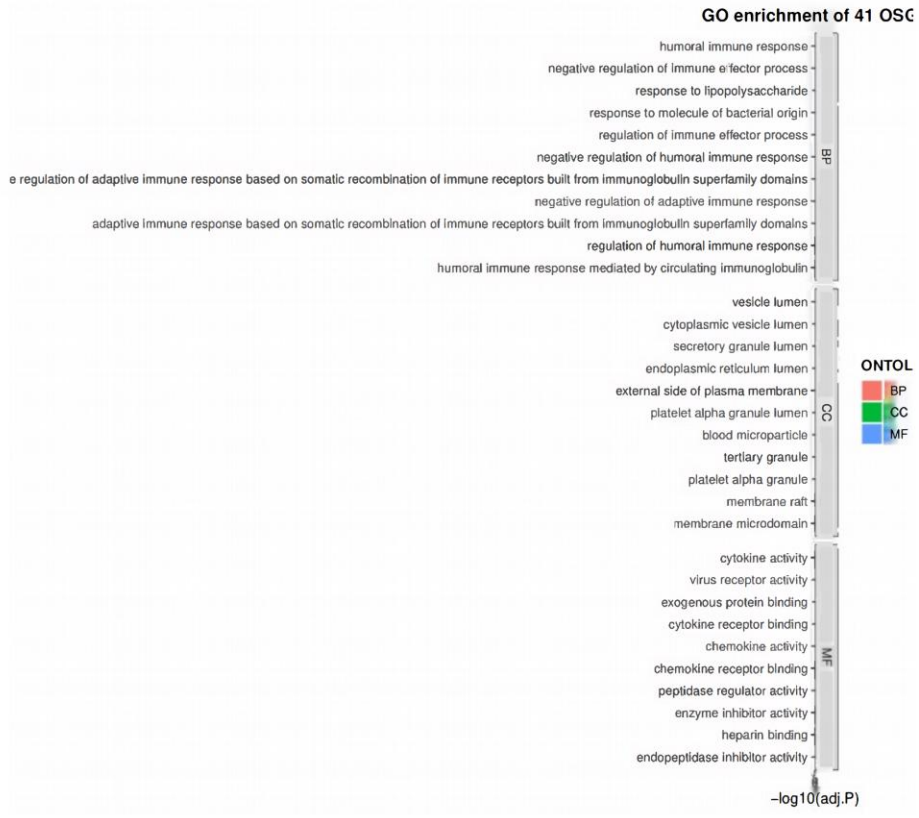


Figure 4. NPC-specific OSGs. (A) Venn diagram of 1,398 GeneCards OSGs and 722 DEGs; (B) expression heatmap of the 67 overlapping OSGs (36 up- and 31 down-regulated); (C) volcano plot highlighting the OSGs.

A


GO enrichment of 41 OSG
humoral immune response
negative regulation of immune effector process
response to lipopolysaccharide
response to molecule of bacterial origin
regulation of immune effector process
negative regulation of humoral immune response
e regulation of adaptive immune response based on somatic recombination of immune receptors built from immunoglobulin superfamily domains
negative regulation of adaptive immune response
adaptive immune response based on somatic recombination of immune receptors built from immunoglobulin superfamily domains
regulation of humoral immune response
humoral immune response mediated by circulating immunoglobulin
BP
vesicle lumen
cytoplasmic vesicle lumen
secretory granule lumen
endoplasmic reticulum lumen
external side of plasma membrane
platelet alpha granule lumen
blood microparticle
tertiary granule
platelet alpha granule
membrane raft
membrane microdomain
CC
cytokine activity
virus receptor activity
exogenous protein binding
cytokine receptor binding
chemokine activity
chemokine receptor binding
peptidase regulator activity
enzyme inhibitor activity
heparin binding
endopeptidase inhibitor activity
MF
ONTOL
BP
CC
MF
−log10(adj.P)

B

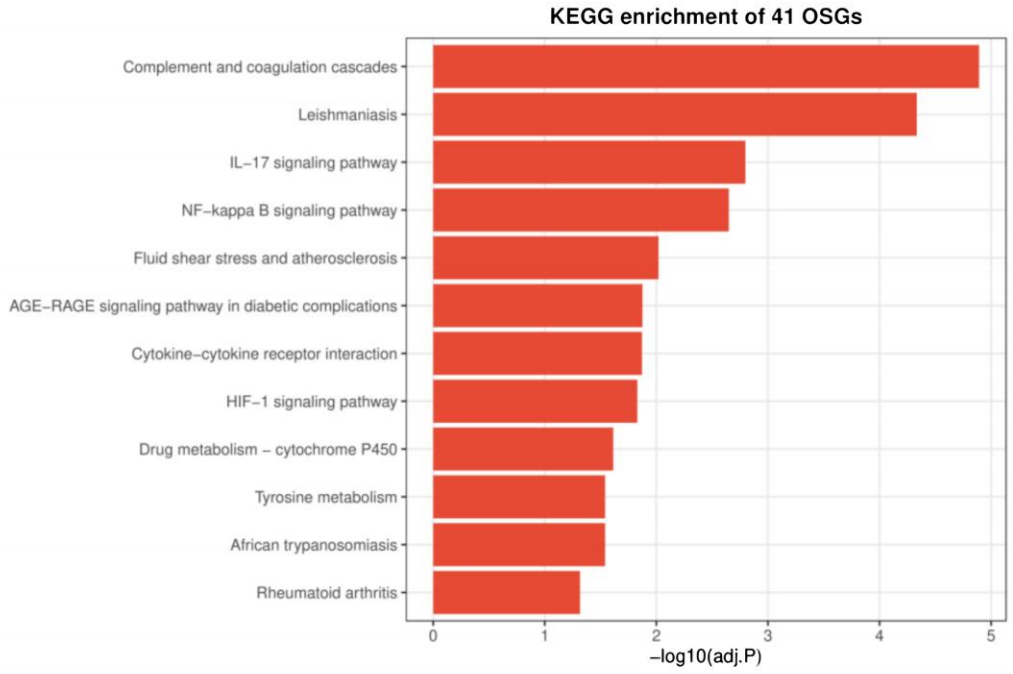

KEGG enrichment of 41 OSGs
Complement and coagulation cascades
Leishmaniasis
IL−17 signaling pathway
NF−kappa B signaling pathway
Fluid shear stress and atherosclerosis
AGE−RAGE signaling pathway in diabetic complications
Cytokine−cytokine receptor interaction
HIF−1 signaling pathway
Drug metabolism − cytochrome P450
Tyrosine metabolism
African trypanosomiasis
Rheumatoid arthritis
0
1
2
3
4
5
−log10(adj.P)

Figure 5. Enrichment of the 67 NPC-specific OSGs. (A) GO (humoral immune response, cytokine activity and secretory-granule/vesicle lumen); (B) KEGG (complement and coagulation cascades, and IL-17, NF-κB and HIF-1 signaling).

3.4 BCHE carries the strongest prognostic signal; FOXM1 defines a high-risk subgroup

In the 88-patient GSE102349 cohort (16 progression events, 72 censored; follow-up 3.2–55.2 months), 14 of the 67 NPC-specific OSGs were associated with survival at univariate Cox $P < 0.05$ (Figure 6A). BCHE had the strongest adverse association (HR = 1.85, 95% CI 1.16–2.94, P = 0.0094); FOXM1 was only borderline significant (HR = 1.71, 95% CI 1.00–2.92, P = 0.0497). With 16 events, a LASSO-Cox step was used to remove collinear and redundant predictors before multivariable modeling. The 14 candidates were reduced to eight non-redundant genes (EPAS1, BCHE, IL33, DMD, BRCA1, CXCL9, EZH2 and ANG); FOXM1 was shrunk to zero and dropped. In the multivariable model on these eight genes, BCHE was the only term retained at $P < 0.1$ (HR = 1.65, 95% CI 0.99–2.74, P = 0.055), and none of the remaining genes approached significance (Figure 6B; Supplementary Table S1).

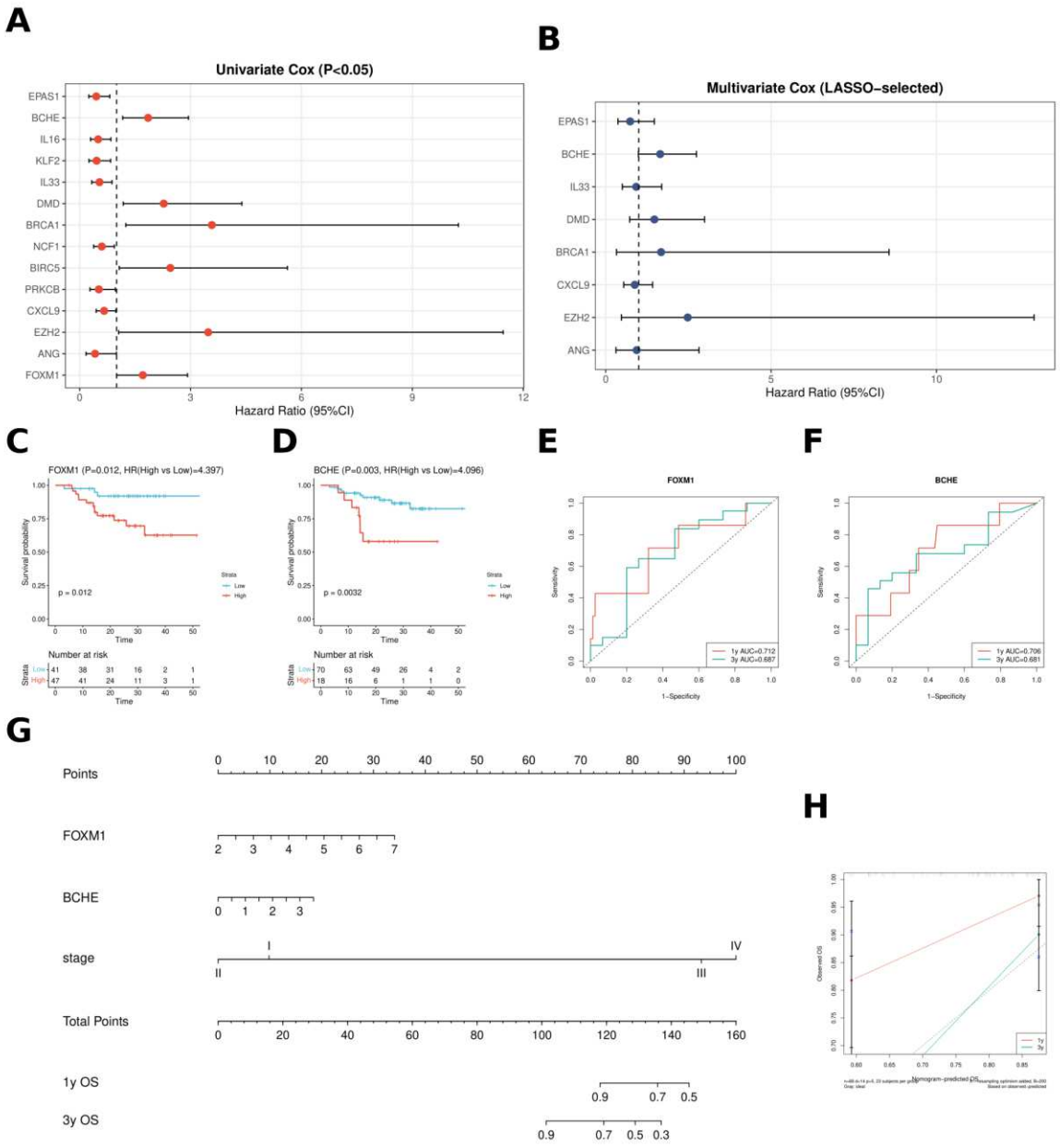


Figure 6. Prognostic value of hub OSGs in GSE102349 (n = 88; 16 events). (A) Univariate and (B) LASSO-selected multivariate Cox forest plots; (C, D) Kaplan–Meier curves for FOXM1 and BCHE (both optimal-cutoff high- vs low-expression splits; both significant); (E, F) time-dependent ROC at 1 and 3 years; (G) stage-inclusive nomogram (n = 68); (H) calibration curves.

Kaplan–Meier analysis with the optimal expression cutoff (surv_cutpoint) confirmed both genes as survival stratifiers. High BCHE tracked with markedly poorer survival (log-rank P = 0.003; high-versus-low HR = 4.10; Figure 6D), and high FOXM1 likewise marked a high-risk subgroup (P = 0.012; HR = 4.40; Figure 6C). The evidence for BCHE

is the more complete: it survived LASSO and multivariable modeling, whereas FOXM1 was zeroed by LASSO and did not persist after adjustment. We therefore treat FOXM1 as a proliferation/E2F-linked marker enriched in malignant cells, whose unadjusted survival signal is largely explained by correlated cell-cycle programs, rather than as an independent predictor (Sections 3.6–3.7 and single-cell analyses).

3.5 Predictive performance and a prognostic nomogram

Time-dependent ROC at 1 and 3 years (5-year estimates were unreliable given shorter follow-up) showed moderate and similar discrimination for both markers: AUC = 0.712 at 1 year and 0.687 at 3 years for FOXM1, and 0.706 and 0.681 for BCHE (Figure 6E,F). A nomogram combining BCHE, FOXM1 and clinical stage was built on the 68 patients with known stage, predominantly III–IV (Figure 6G). Its C-index was 0.747, or 0.679 after bootstrap correction, and calibration curves showed acceptable agreement between predicted and observed 1- and 3-year survival (Figure 6H).

3.6 External validation across independent NPC cohorts and at single-cell resolution

Both hub genes were concordantly up-regulated in NPC across the three independent microarray cohorts (Figure 7A–F). FOXM1 logFC was 0.89 in GSE12452 ($P = 6.9 \times 10^{-6}$), 1.61 in GSE53819 ($P = 3.4 \times 10^{-5}$) and 1.53 in GSE64634 ($P = 0.078$); BCHE logFC was 0.65 ($P = 0.053$), 1.49 ($P = 0.034$) and 1.20 ($P = 0.26$), respectively (Wilcoxon). The direction was the same in all six comparisons. Significance was not reached in GSE64634, which contains only 12 tumors and four controls, or for BCHE in GSE12452; both are borderline findings consistent with limited power. Because the Human Protein Atlas does not include NPC and NPC-specific immunohistochemistry could not be obtained, GSE150430 was used for cell-resolved validation (Figure 7G,H). Both genes were strongly enriched in malignant cells compared with non-malignant epithelial cells: FOXM1 mean expression 0.109 versus 0.019 (24.3% versus 4.4% expressing cells) and BCHE 0.090 versus 0 (20.2% versus 0%), with Wilcoxon $P < 2.2 \times 10^{-16}$ for both (7,581 versus 666 cells). Both signals thus localize to the malignant compartment, adding cell-level support to the bulk findings.

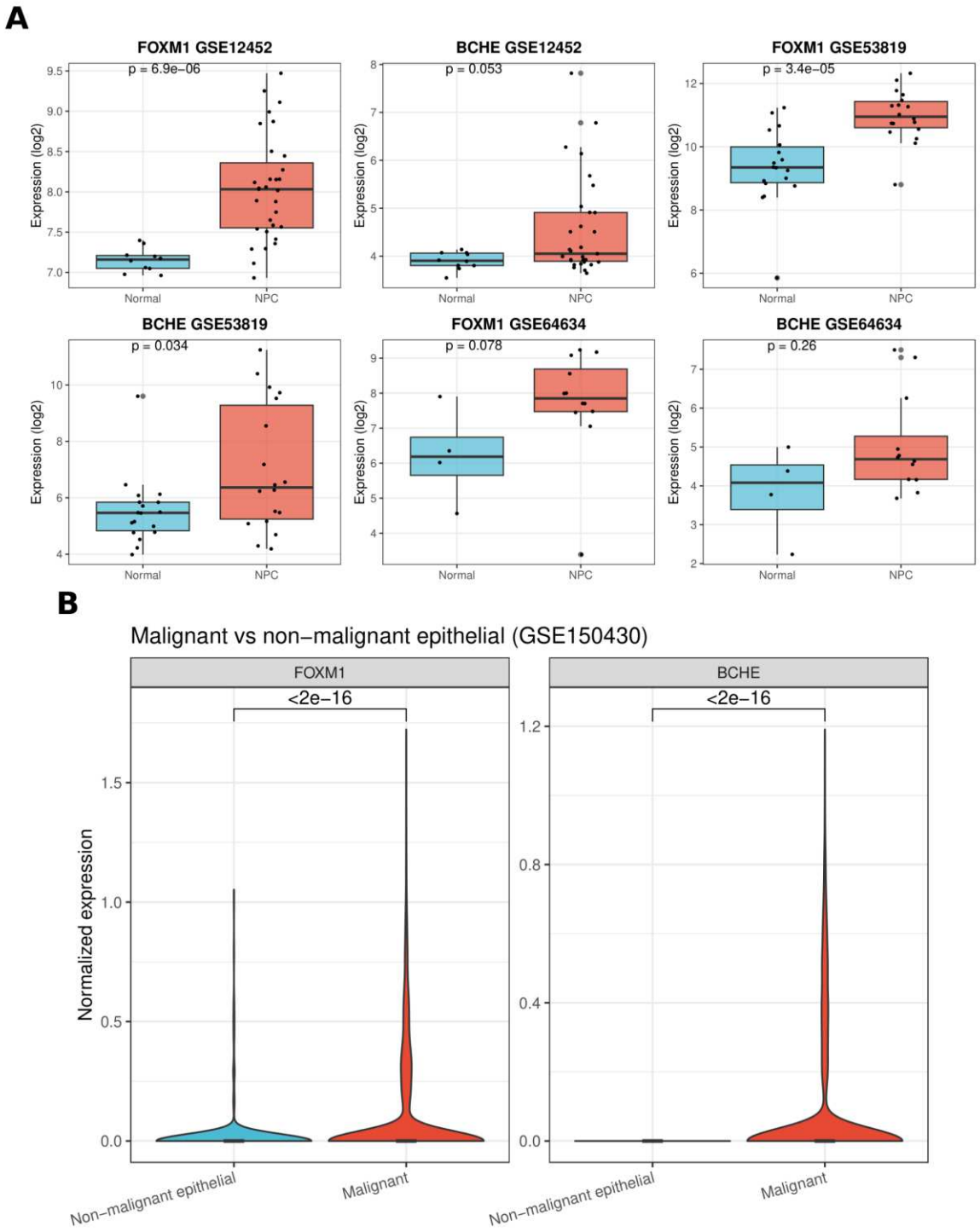


Figure 7. External expression validation. (A–F) FOXM1 and BCHE boxplots across GSE12452, GSE53819 and GSE64634 (NPC vs normal nasopharynx, Wilcoxon; logFC and P indicated); (G, H) single-cell (GSE150430) violin/box plots comparing malignant with non-malignant epithelial cells for FOXM1 and BCHE (Wilcoxon). NPC immunohistochemistry is not shown because the Human Protein Atlas pathology atlas does not include nasopharyngeal carcinoma.

3.7 GSEA links FOXM1 and BCHE to proliferation and EMT programs

Hallmark GSEA on Spearman-ranked genes (nominal $P < 0.05$, FDR < 0.25) revealed two distinct but complementary programs (Figure 8). FOXM1 covaried most strongly with cell-cycle and proliferation pathways: E2F targets (NES = 4.05), MYC targets v1 and v2 (NES = 3.84 and 3.32), the G2M checkpoint (3.68), mTORC1 signaling, mitotic spindle and DNA repair (all FDR $\approx 4.2 \times 10^{-10}$). It was inversely associated with interferon-γ/α response, allograft rejection and complement (NES from −2.4 to −3.0). BCHE gave the mirror-image immune pattern, with strong negative enrichment of interferon-γ response (NES = −3.52), allograft rejection (−3.22), interferon-α response (−3.18), complement (−2.77), inflammatory response and IL-6/JAK/STAT3 signaling, alongside positive enrichment of Wnt/β-catenin signaling (NES = 2.28), epithelial–mesenchymal transition (2.24) and Hedgehog signaling. FOXM1 thus marks a proliferative, immune-quiet program, and BCHE an EMT/Wnt state equally depleted of cytotoxic, interferon-driven immunity.

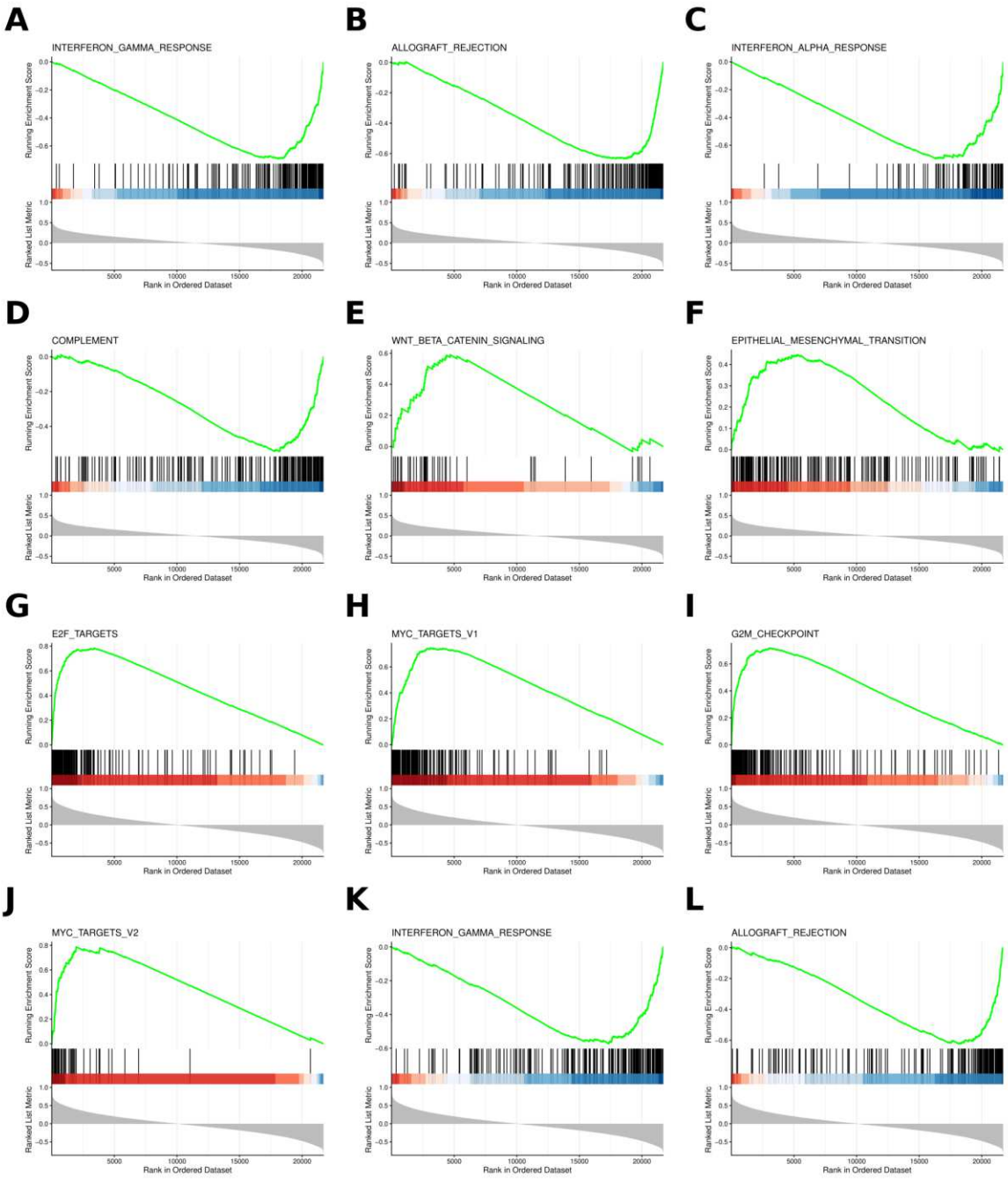


Figure 8. Hallmark GSEA of genes ranked by co-variation with each hub gene. (A–F) BCHE: negative enrichment of interferon-γ/α response, allograft rejection and complement, with positive enrichment of Wnt/β-catenin signaling and EMT; (G–L) FOXM1: positive enrichment of E2F targets, MYC targets and the G2M checkpoint, with negative enrichment of interferon-γ response and allograft rejection.

3.8 NPC displays a remodeled immune-cell composition

All 93 deconvolved samples, 61 NPC and 32 normal, passed the CIBERSORT P < 0.05 filter (1,000 permutations). Twelve of the 22 subsets differed at nominal P < 0.05, and 11 remained significant after Benjamini–Hochberg correction (Figure 9A). NPC showed depletion of naïve B, memory B, naïve CD4 T and resting memory CD4 T cells, with enrichment of plasma cells, activated memory CD4 T cells, activated NK cells, M0 and M1 macrophages, resting dendritic cells and neutrophils. Pairwise correlations among the 22 subsets revealed coordinated modules (Figure 9B), and stacked composition plots showed the extent of remodeling (Figure 9C).

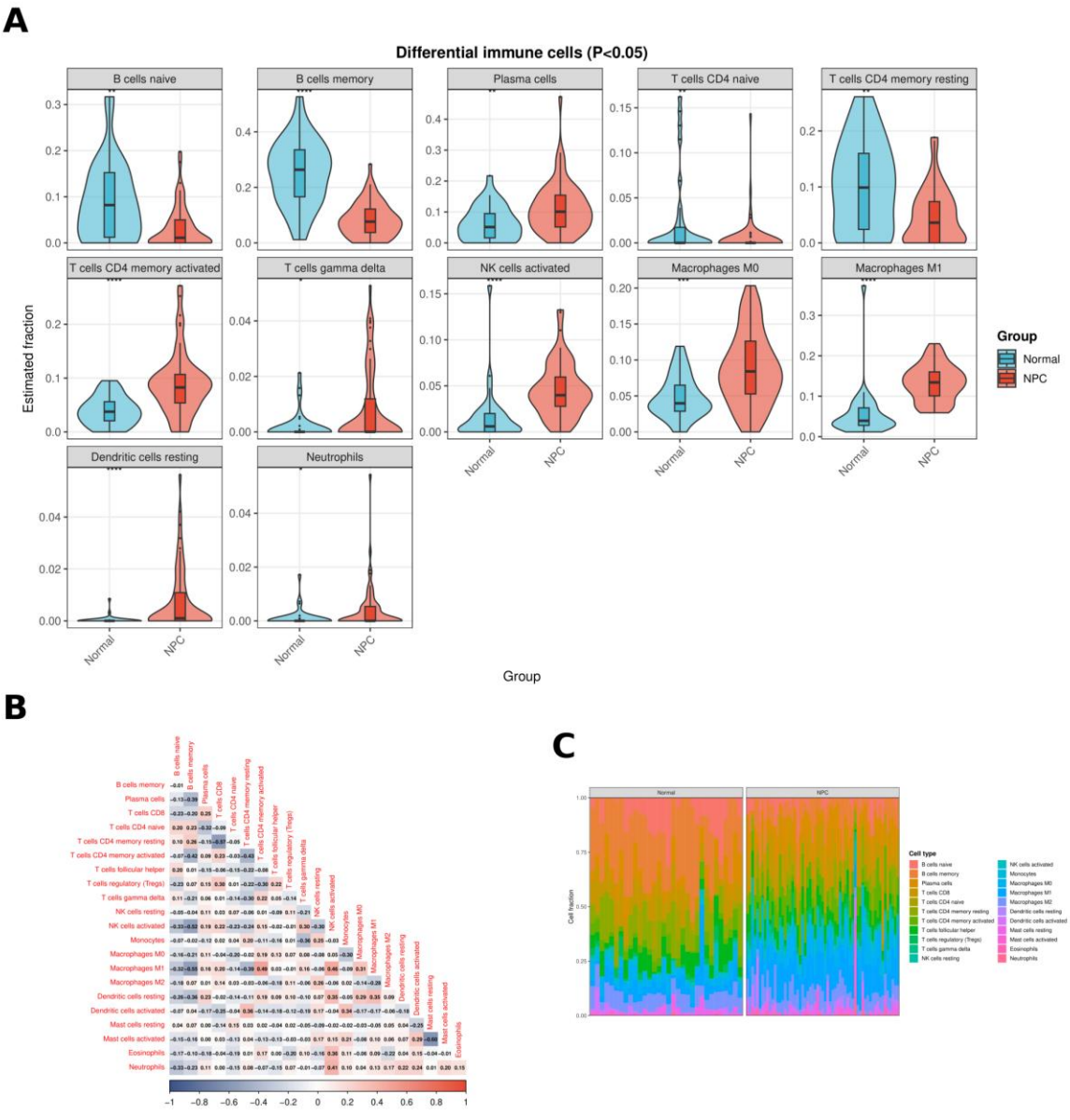


Figure 9. CIBERSORT immune-cell composition. (A) violin/box plots of significantly differential subsets; (B) subset correlation heatmap; (C) stacked composition bar plot.

3.9 A ten-cell LASSO immune signature

LASSO logistic regression on the 22 immune fractions, at lambda.min, selected a small set of discriminative subsets (Figure 10A,B). Their overlap with the significantly differential subsets produced a ten-cell signature: naïve B, memory B, naïve CD4 T, resting and activated memory CD4 T, gamma-delta T, M0 and M1 macrophages, resting dendritic cells and neutrophils (Figure 10C). A heatmap of these ten fractions separated NPC from normal tissue.

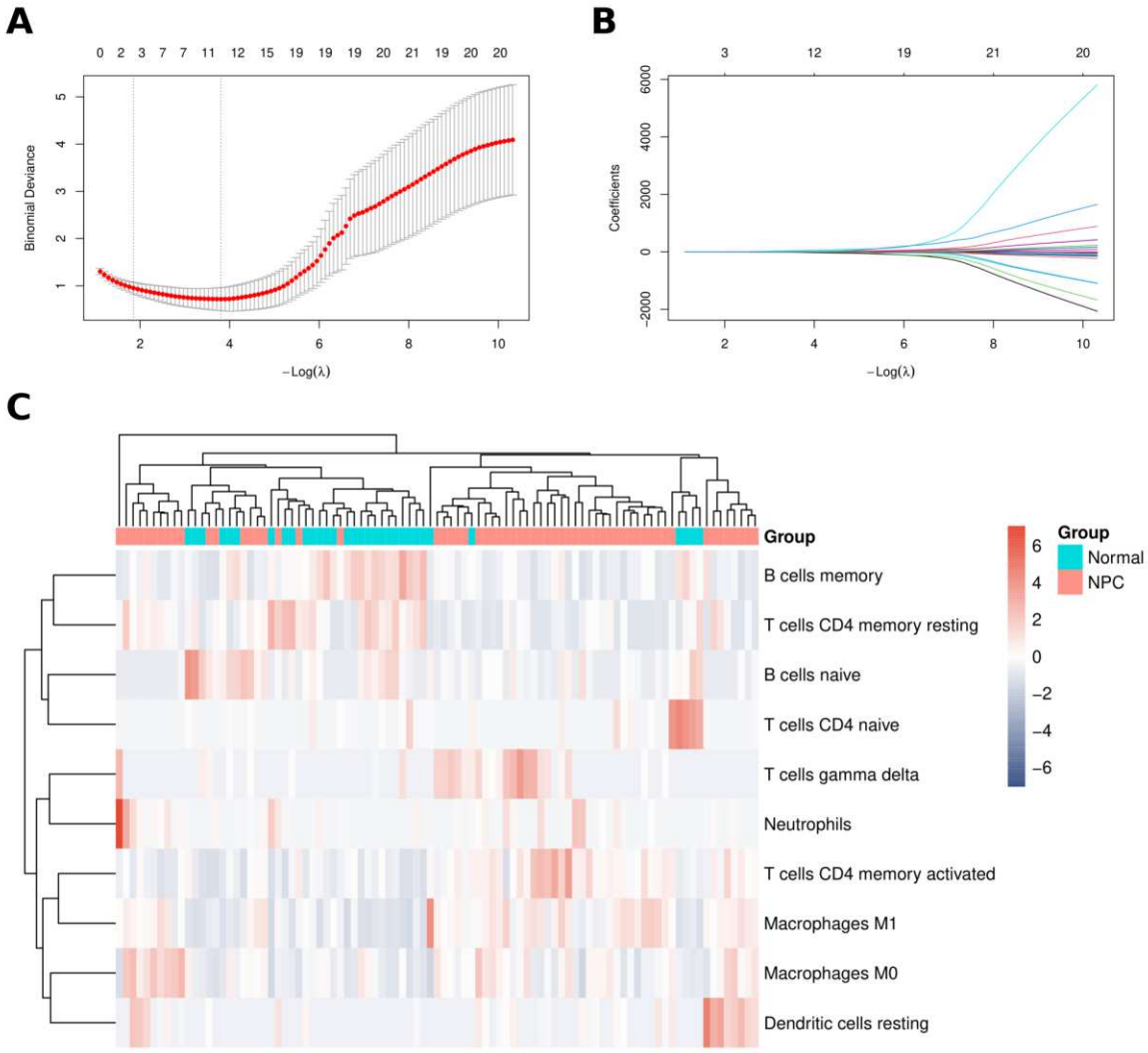


Figure 10. LASSO immune signature. (A) cross-validation curve; (B) coefficient path; (C) heatmap of the final ten-cell signature.

3.10 Hub genes correlate with immune subsets and checkpoints

Across the 93 samples (Figure 11A), FOXM1 correlated most strongly and positively with M1 macrophages ($r = 0.47$, $P = 2.9 \times 10^{-6}$), M0 macrophages ($r = 0.42$, $P = 2.3 \times 10^{-5}$) and resting dendritic cells ($r = 0.33$, $P = 0.0013$), and negatively with memory B cells ($r = -0.42$, $P = 2.8 \times 10^{-5}$) and resting memory CD4 T cells ($r = -0.29$, $P = 0.0044$). BCHE showed a similar pattern, with positive correlations to M0 macrophages ($r = 0.28$, $P = 0.0057$), resting dendritic cells ($r = 0.26$, $P = 0.011$) and M1 macrophages ($r = 0.25$, $P = 0.016$). The two hubs were themselves positively correlated ($r = 0.39$, $P = 1.4 \times 10^{-4}$) (Figure 11B–D). For checkpoints, FOXM1 correlated with CD274/PD-L1 ($r = 0.24$, $P = 0.020$) and TNFRSF9 ($r = 0.22$, $P = 0.038$), with a trend toward HAVCR2/TIM-3 ($r = 0.20$, $P = 0.061$); BCHE was weakly and inversely related to PDCD1/PD-1 ($r = -0.21$, $P = 0.044$). CTLA4, LAG3 and TIGIT showed no significant association (Figure 11E,F). Modest as they are, these correlations point to an immune-suppressed, checkpoint-responsive compartment in hub-gene-high tumors.

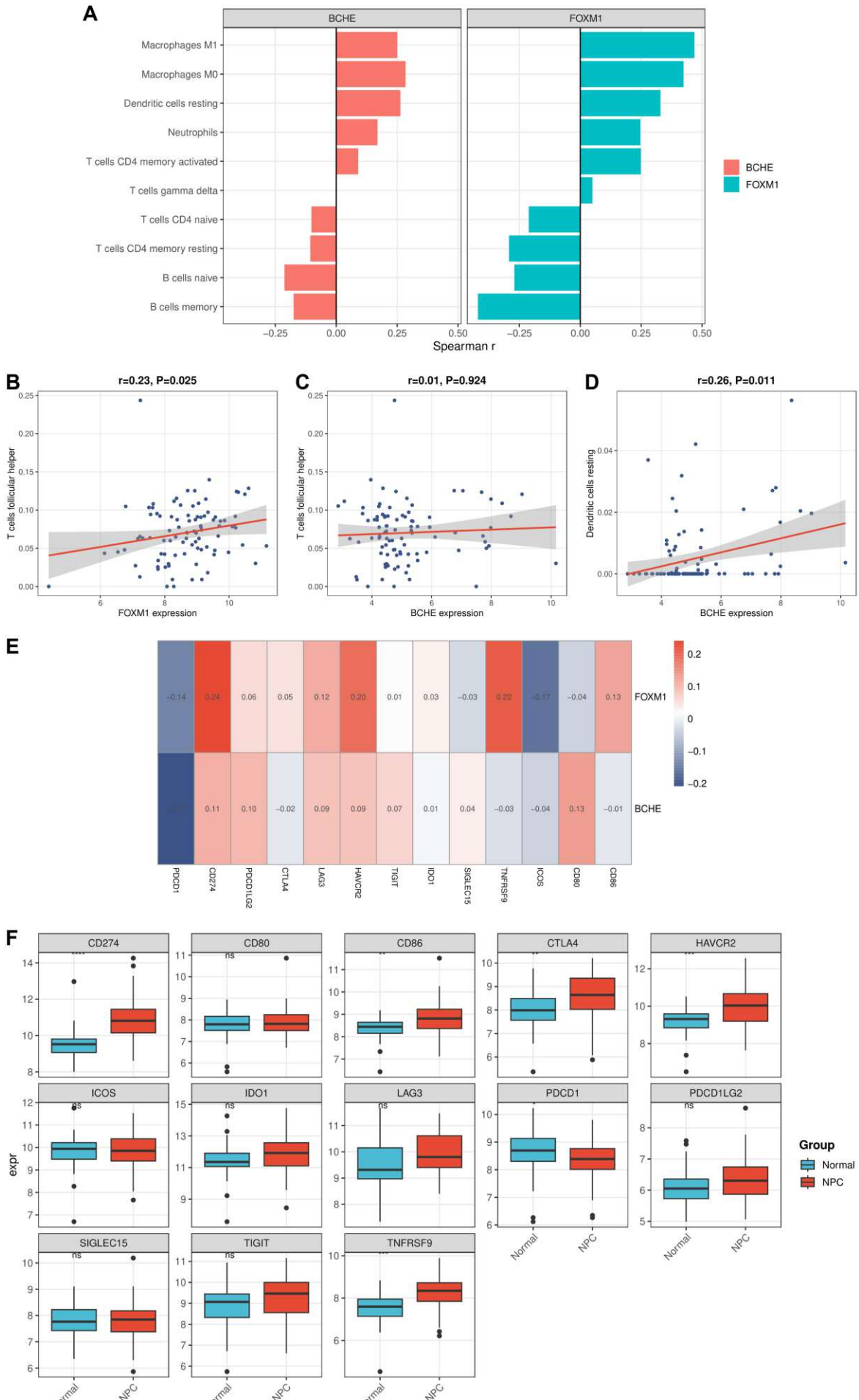

A
BCHE
FOXM1
Macrophages M1
Macrophages M0
Dendritic cells resting
Neutrophils
T cells CD4 memory activated
T cells gamma delta
T cells CD4 naive
T cells CD4 memory resting
B cells naive
B cells memory
−0.25
0.00
0.25
0.50
Spearman r
BCHE
FOXM1
B
r=0.23, P=0.025
T cells follicular helper
FOXM1 expression
C
r=0.01, P=0.924
T cells follicular helper
BCHE expression
D
r=0.26, P=0.011
Dendritic cells resting
BCHE expression
E
−0.14
0.24
0.06
0.05
0.12
0.20
0.01
0.03
−0.03
0.22
−0.17
−0.04
0.13
FOXM1
0.11
0.10
−0.02
0.09
0.09
0.07
0.01
0.04
−0.03
−0.04
0.13
−0.01
BCHE
0.2
0.1
0
−0.1
−0.2
PDCD1
CD274
PDCD1LG2
CTLA4
LAG3
HAVCR2
TIGIT
IDO1
SIGLEC15
TNFRSF9
ICOS
CD80
CD86
F
CD274
CD80
CD86
CTLA4
HAVCR2
ICOS
IDO1
LAG3
PDCD1
PDCD1LG2
SIGLEC15
TIGIT
TNFRSF9
ns
expr
Normal
NPC
Group
Normal
NPC

Figure 11. Gene–immune and checkpoint correlations. (A) lollipop plot of FOXM1/BCHE vs signature subsets; (B–D) representative Spearman scatter plots; (E) gene–checkpoint correlation heatmap; (F) checkpoint expression boxplots.

3.11 ssGSEA and predicted drug sensitivity

Independent ssGSEA of 28 immune populations supported the CIBERSORT results, with 17 populations differing after Benjamini–Hochberg correction (Figure S2). Activated and effector T-cell states (activated CD4, central-memory CD8, effector-memory CD4, Th2, Th17 and regulatory T cells), macrophages, NK and NKT cells were higher in NPC; activated and immature B cells, central-memory CD4 T cells, CD56bright NK cells, eosinophils, monocytes, and immature and plasmacytoid dendritic cells were lower. pRRophetic predicted differential sensitivity to six agents (adjusted $P < 0.05$). Cisplatin, docetaxel, gemcitabine, etoposide and cytarabine had lower predicted IC50 in NPC, indicating greater sensitivity, while mitomycin C showed the opposite; paclitaxel, doxorubicin, bleomycin and erlotinib did not differ (Figure S3; Supplementary Table S2). These predictions require experimental confirmation.

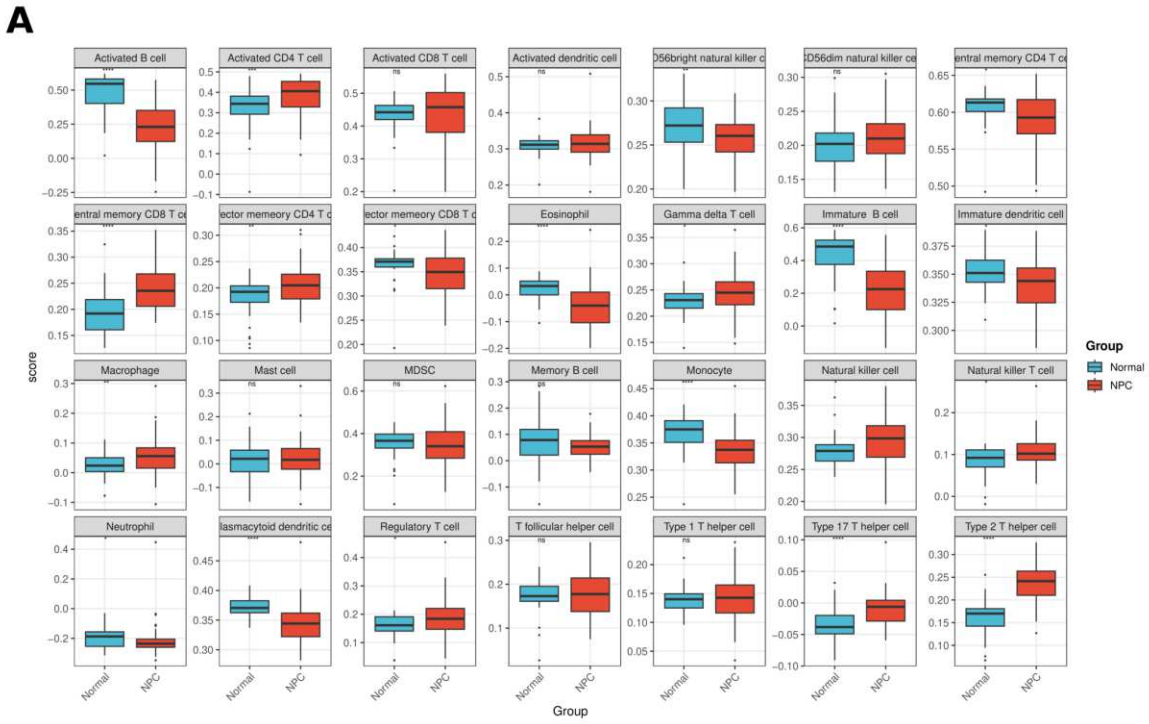


Figure S2. ssGSEA scores of 28 immune populations (NPC vs normal).

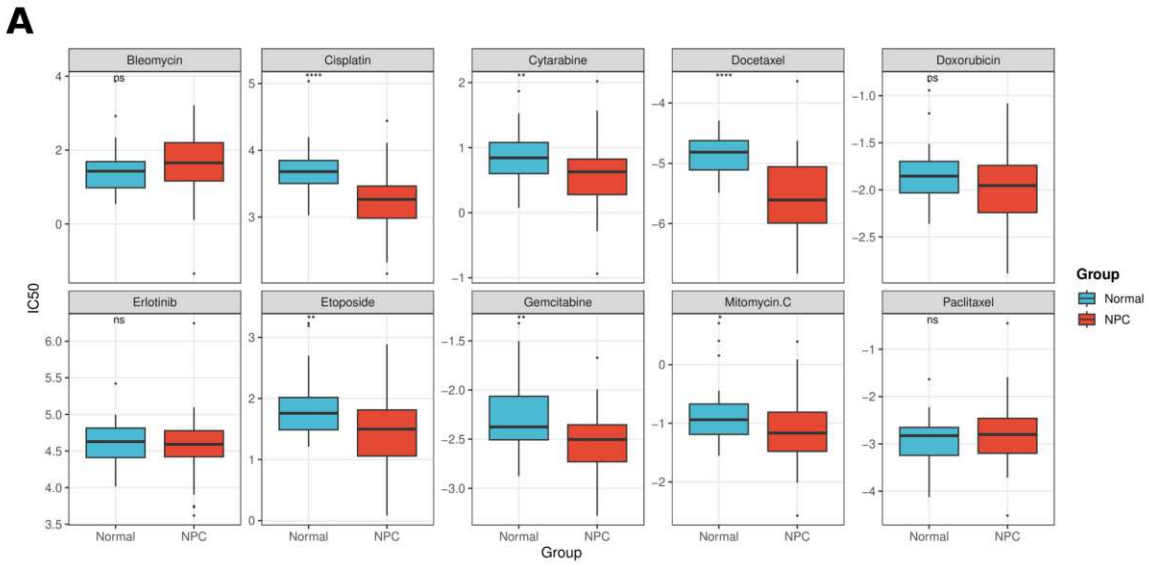


Figure S3. pRRophetic predicted IC50 for candidate drugs (NPC vs normal).

3.12 Single-cell expression of FOXM1 and BCHE

GSE150430 contained 48,584 cells, 46,001 from NPC and 2,583 from normal nasopharynx, partitioned by the original authors into 26 annotated clusters that included malignant cells (n = 7,581), non-malignant epithelial cells, CAFs, and the full range of T, B, plasma, myeloid, NK and dendritic populations (Figure S4A). Both hub genes concentrated in malignant cells. FOXM1 was detected in 24.3% of malignant cells (mean expression 0.109) but only 4.4% of non-malignant epithelial cells (mean expression 0.019; Wilcoxon $P < 2.2 \times 10^{-16}$, 7,581 versus 666 cells), with weaker signal in proliferative B and dysregulated $CD8^{+}$ T cells. BCHE was expressed in 20.2% of malignant cells (mean expression 0.090) and was essentially absent from non-malignant epithelial cells (0%; $P < 2.2 \times 10^{-16}$) and from most stromal and immune populations (Figure S4B–E; Supplementary Table S3). At single-cell resolution, then, both genes are predominantly tumor-cell intrinsic. This localizes the bulk prognostic signal of BCHE to malignant cells and supports FOXM1 as a marker of the proliferative malignant state.

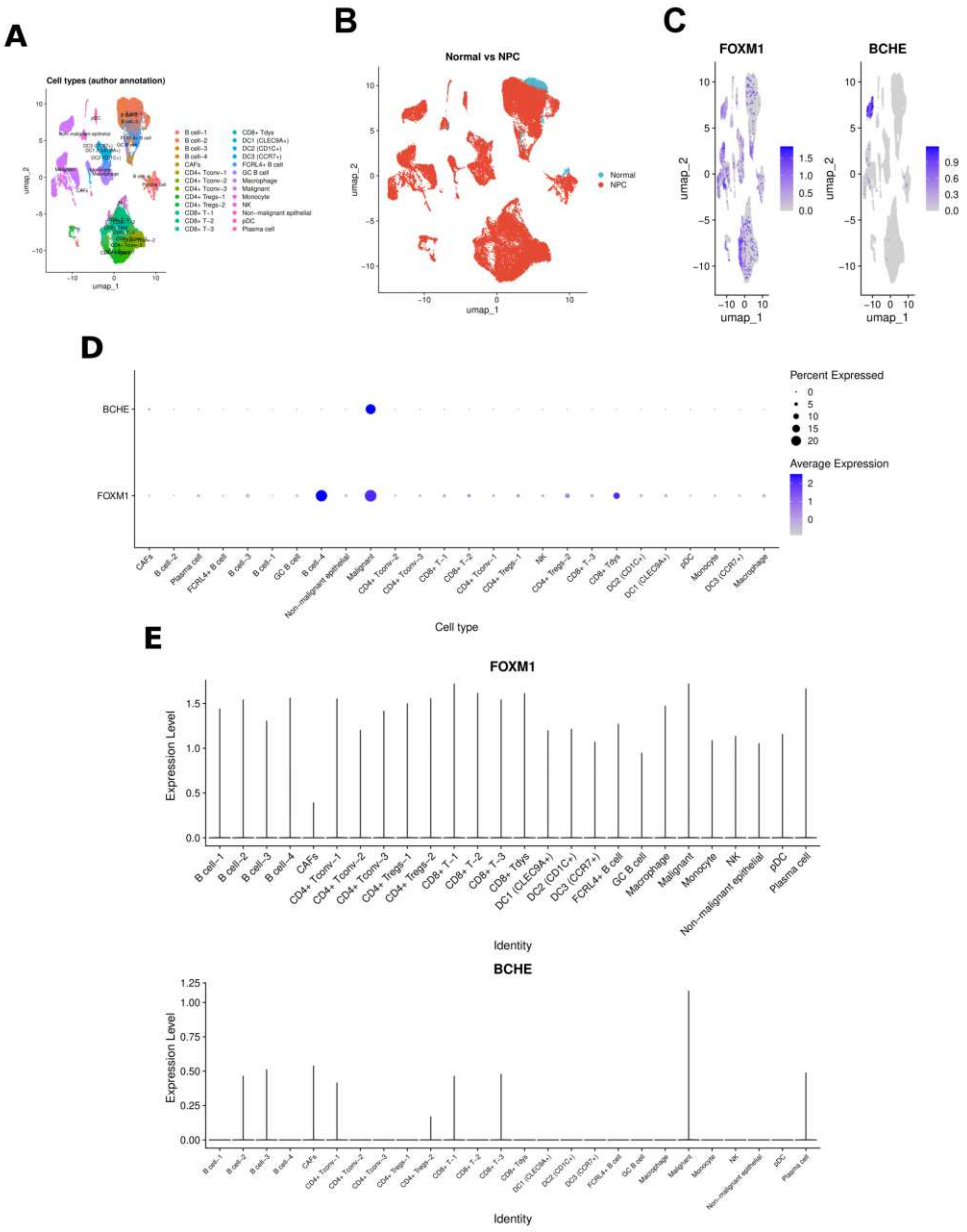


Figure S4. Single-cell validation in GSE150430 (48,584 cells, 26 author-annotated clusters; 46,001 NPC vs 2,583 normal). (A) UMAP colored by cell type and (B) by normal-vs-NPC origin; (C) FOXM1/BCHE FeaturePlot; (D) DotPlot; (E) VlnPlot across cell types. Both genes peak in malignant cells.

3.13 In silico perturbation, co-expression modules and TF regulon activity

We next asked how the malignant network would respond to losing either hub, moving beyond simple co-localization. scTenifoldKnk was applied to the 7,581 malignant cells. GSE150430 stores log1p(CP10K) values (column sums equal 10,000 after expm1), so the matrix was back-transformed to the linear scale before ten bootstrap

gene-regulatory networks were compared between wild-type and virtual-knockout (KO) states by manifold alignment (Figure S5A–D). The knocked gene was, in each case, the dominant perturbed node. After excluding it, 288 genes in the FOXM1-KO and 286 in the BCHE-KO exceeded $|Z| = 1.5$. The shared leading candidates were MALAT1 ($Z \approx 2.16$, nominal $P = 0.013$), NPM1, CD74, ribosomal and HLA genes, and their GO enrichment converged on MHC-II protein-complex and peptide-antigen assembly and antigen processing (adjusted $P \approx 10^{-13}$ to 10^{-16}) (Figure S5C,D). On this already-integrated matrix, adjusted signals were conservative: only the knocked gene passed FDR < 0.05 under either the theoretical or Efron empirical null, and the two KOs produced overlapping network responses. The KO results are treated as hypothesis-generating and were supplemented by a correlation-based module analysis that does not rely on network resampling. Among malignant cells, the top 300 positive co-expression partners of each hub showed coherent enrichment (Figure S5E). The FOXM1 module, led by BIRC5, UBE2C, TK1, MKI67, NUSAP1 and TOP2A, was dominated by mitosis, chromosome segregation, nuclear division and cell-cycle-phase transition terms (chromosome segregation, adjusted $P = 2.0 \times 10^{-63}$; mitotic nuclear division, 4.5×10^{-59}). The BCHE module (CSRNP3, OCA2, CLDN3 and HLA-DQA2) was enriched for ribosome biogenesis (4.1×10^{-13}) and MHC-II/peptide-antigen assembly. For regulation, DoRothEA regulons (confidence A–C, 271 transcription factors) were scored per cell with viper as a lightweight SCENIC-style analysis (Figure S6A,B). The FOXM1 regulon was high in malignant cells (mean activity 0.72) and far above non-malignant epithelial cells (−0.65), sharing a high-activity tier with proliferating B cells, dysregulated CD8 T cells and plasma cells, as expected for a cell-cycle transcription factor. Across the key-regulator panel, malignant cells had the highest activity for MYC (1.18), FOXM1 (0.72), HIF1A (0.55) and MYBL2 (0.34) and the lowest for the interferon-associated STAT1 (−2.57), reproducing the bulk GSEA pattern of MYC/E2F enrichment and IFN-γ suppression at single-cell level. Perturbation, co-expression and regulon evidence converge on FOXM1 as an upstream driver of a proliferative MYC/E2F/G2M program, while BCHE marks a translationally active, antigen-presenting malignant substate. Cell-type-matched NPC-versus-normal regulon comparisons are not reported: most normal populations contained two cells or fewer.

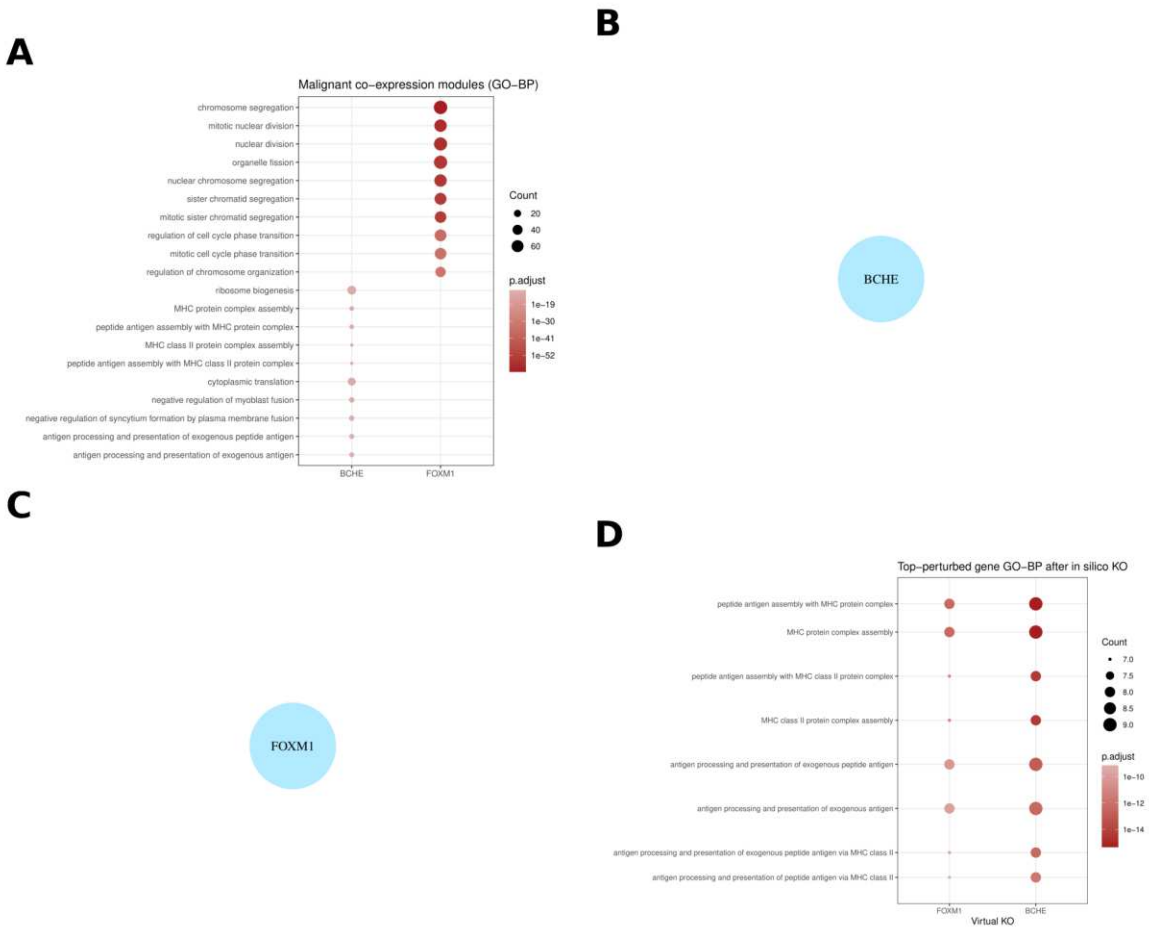


Figure S5. In silico knockout and malignant co-expression modules. (A, B) scTenifoldKnk WT-vs-KO manifold-alignment plots for FOXM1 and BCHE within malignant cells (linear-scale matrix, ten bootstrap networks), with the most perturbed genes labeled; (C, D) ranked perturbation Z plots and GO-BP enrichment of the top-60 perturbed genes (MHC-II assembly/antigen processing; on this integrated matrix only the knocked gene passes FDR < 0.05, so these are reported as hypothesis-generating); (E) GO-BP dot plot of the top-300 positive co-expression modules of FOXM1 (mitosis/chromosome segregation) and BCHE (ribosome biogenesis/MHC-II assembly) within malignant cells.

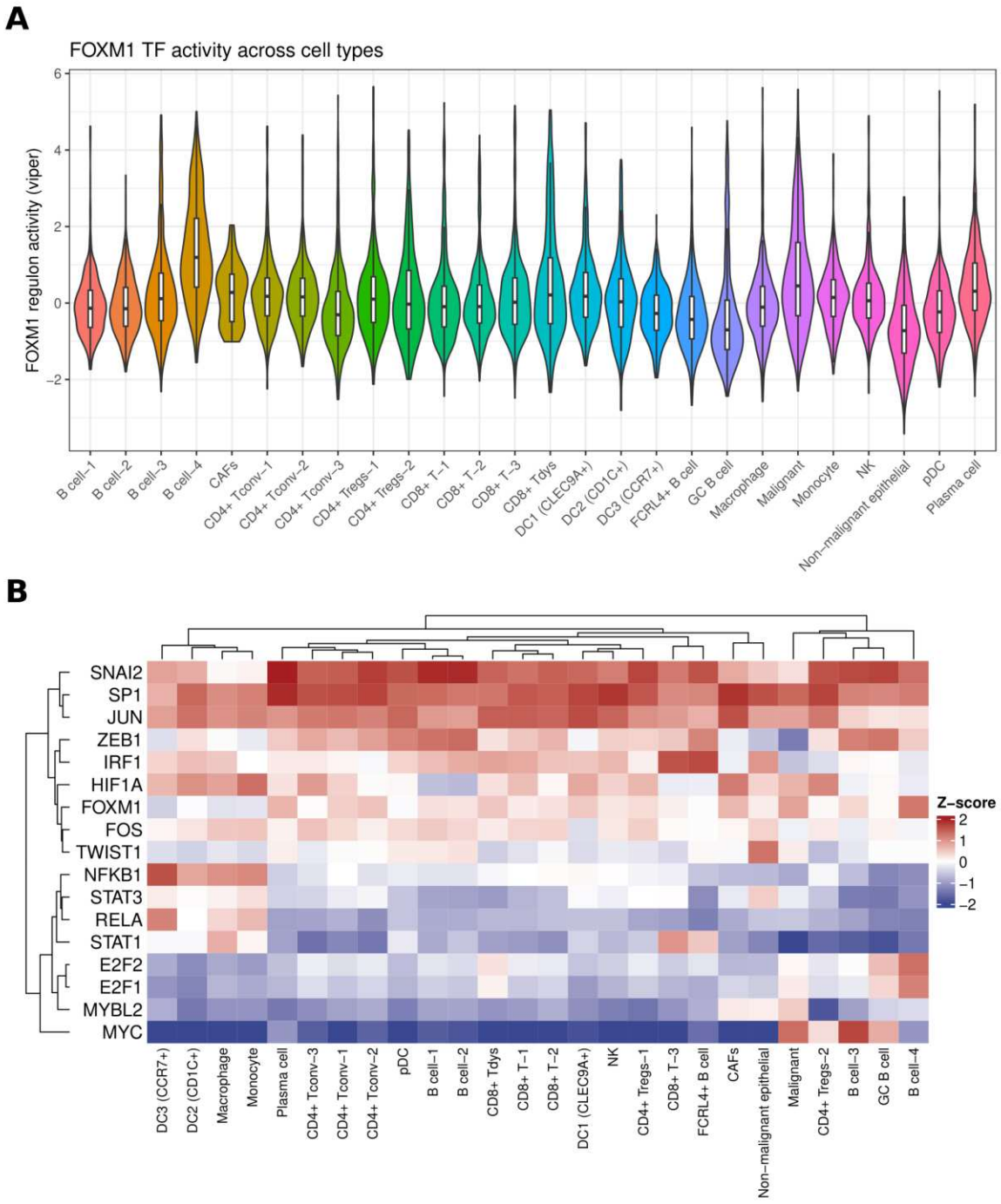


Figure S6. Single-cell transcription-factor regulon activity (DoRothEA A–C, 271 regulons; viper). (A) FOXM1 regulon activity by cell type (violin/boxplot; high in malignant cells and other proliferative populations, lowest in non-malignant epithelium); (B) z-scored heatmap of proliferation/EMT/inflammatory regulators across cell types (malignant cells high in MYC/FOXM1/HIF1A/MYBL2, low in STAT1).

3.14 Malignant-state trajectory and intratumoral cell–cell communication

We then examined how malignant cells arrange along a state continuum and how they interact with surrounding populations. Monocle3 ordered all 7,581 malignant cells into 14 substates (pseudotime 0–57.6), and slingshot on the same subclusters produced a concordant trajectory (Spearman $|r| = 0.772$; only the sign differs because the two methods anchor opposite ends) (Figure 13A). Both hub genes were enriched at the same low-pseudotime pole and declined along the trajectory: BCHE mean expression fell from 0.353 in the earliest quartile to 0.0008 in the latest, and FOXM1 from 0.180 to 0.042 (Figure 13B). FOXM1 and BCHE therefore mark a shared early malignant substate rather than separate branches. CellChat was run on the NPC microenvironment (9,821 cells after capping each population at 400; normal tissue had no malignant cells and too few myeloid cells for a matched contrast), recovering 10,134 ligand–receptor pairs across 111 pathways (Figure 12A,B). As a sender, the malignant population was dominated by MIF signaling to B, CD8 T, dendritic and macrophage populations (probability 0.21–0.28, permutation $P < 0.001$), with additional GALECTIN and CD70 output toward dysregulated CD8 T cells and APP, CCL and CXCL signals (Figure 12C). As a receiver, it was most exposed to CAF-derived COLLAGEN (probability 0.69), LAMININ and FN1 through ECM–receptor interactions, and to midkine (MK) growth signaling (Figure 12D). CAFs were the strongest overall sender (outgoing weight 26.2) and malignant cells the second (15.9). These links give the bulk findings a cellular basis: malignant cells use MIF, galectin and CD70 circuits that can restrain nearby lymphocytes (33-37), in line with the suppressed IFN-γ response and checkpoint correlations seen in bulk, while CAF-deposited ECM provides the structural setting for the EMT/Wnt program identified by GSEA.

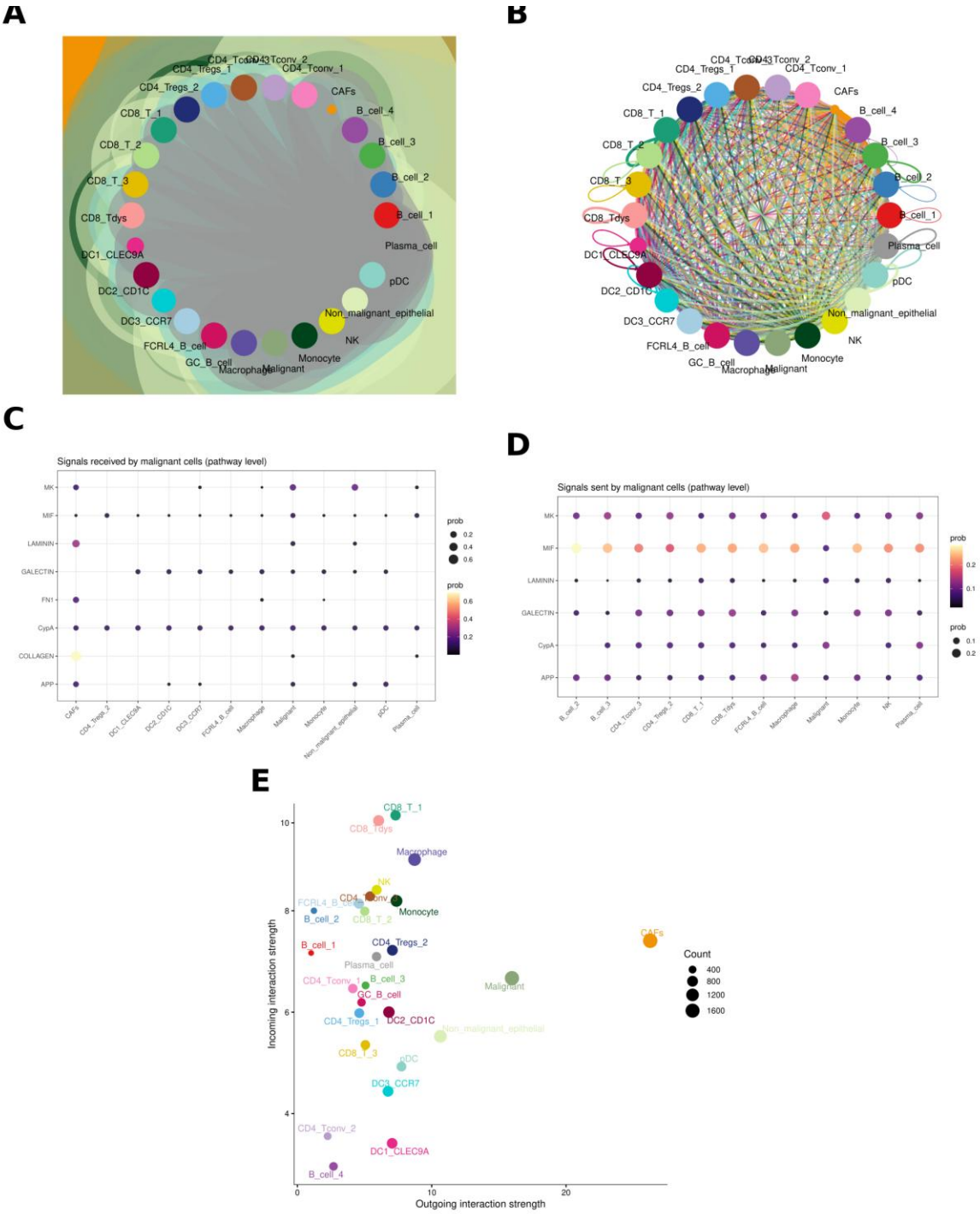


Figure 12. CellChat intratumoral communication in the NPC microenvironment. (A, B) circle plots of interaction number and weight; (C) outgoing and (D) incoming pathway-level bubble plots for malignant cells (MIF, GALECTIN, CD70 outgoing; CAF COLLAGEN/LAMININ/FN1 and MK incoming); (E) outgoing-vs-incoming signaling-role scatter.

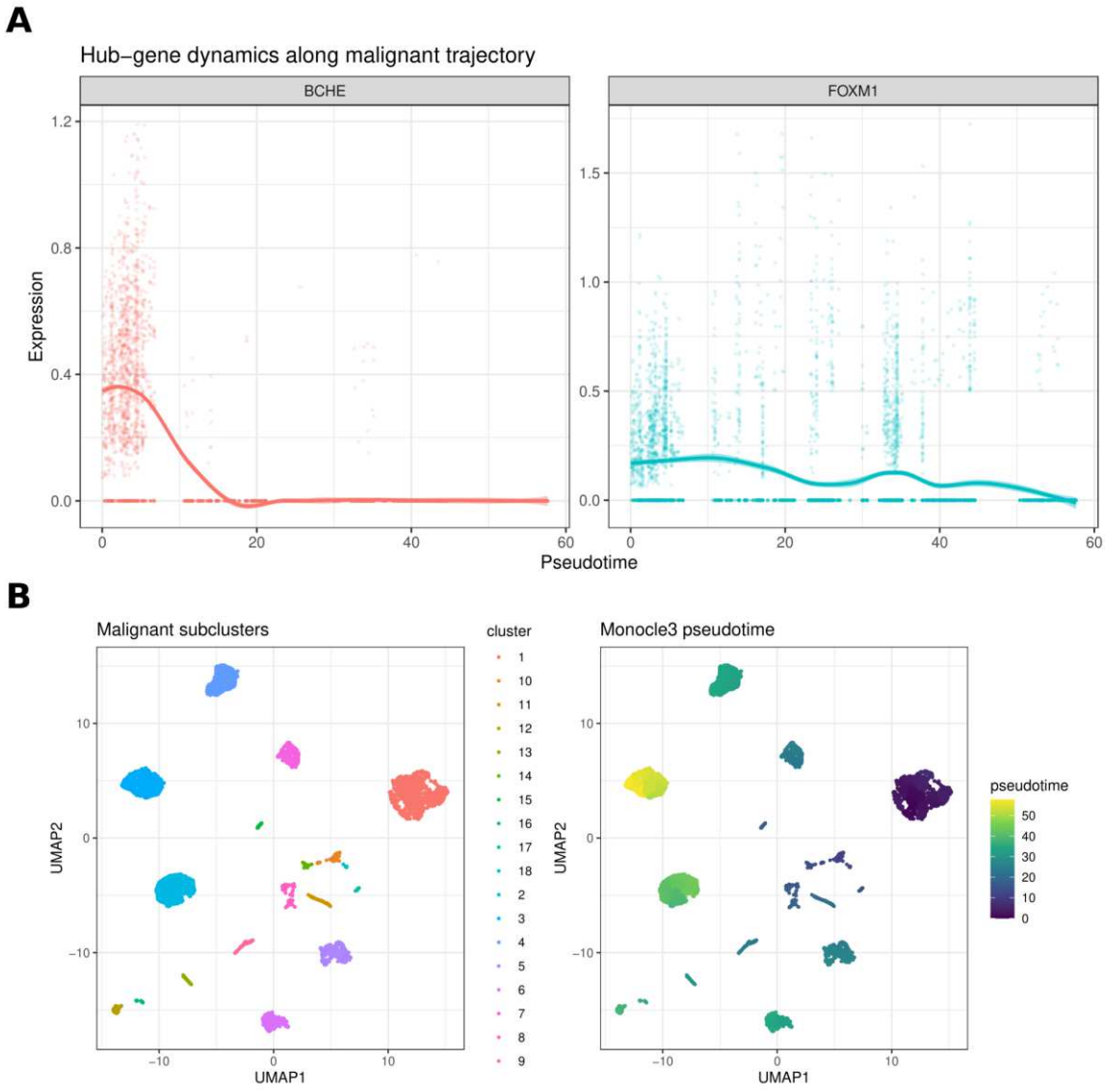


Figure 13. Malignant-cell trajectory. (A) Monocle3 UMAP colored by 14 malignant substates and by pseudotime (slingshot concordance |Spearman r| = 0.772); (B) FOXM1/BCHE expression loess curves across pseudotime quartiles.

4. Discussion

Our two-strategy, multi-cohort workflow points to two OS-related genes with complementary roles in NPC. BCHE carries the strongest and most consistent prognostic signal, while FOXM1 is tied to proliferation and enriched in malignant cells. Combining RRA across datasets with ComBat-corrected limma, and relying on their intersection, reduces the chance of dataset-specific artifacts. The prognostic evidence comes from an independent RNA-seq cohort rather than the discovery datasets.

FOXM1 is a forkhead transcription factor built around the G2/M transition, and an established driver of proliferation, the DNA-damage response and chemoresistance (38). The GSEA results fit this role directly: G2M checkpoint, E2F targets and DNA repair all covaried with FOXM1, and the single-cell data placed the gene in proliferating malignant cells. The connection with oxidative stress is mechanistic rather than incidental. Foxm1-deficient cells accumulate ROS and show elevated oxidative damage, and FOXM1 transcriptionally controls antioxidant and ROS-detoxifying programs, creating a feed-forward loop in which ROS-driven transformation induces FOXM1 and FOXM1 in turn helps tumor cells tolerate the oxidative burden (39). The same logic fits NPC, where FOXM1 promotes proliferation, invasion and stem-cell properties (40), can signal through Wnt/β-catenin (41), and its down-regulation sensitizes cells to cisplatin by disabling MRN–ATM-mediated DNA repair (42); in a clinical NPC series, FOXM1 expression also predicted poorer survival alongside Aurora-B (43). High FOXM1 nonetheless separated a high-risk subgroup in our Kaplan–Meier analysis ($P = 0.012$) without surviving LASSO shrinkage or multivariable adjustment. That pattern is expected for a generic proliferation factor whose information is largely shared with correlated cell-cycle genes, and we present FOXM1 mainly as a mechanistic and malignant-state marker rather than an independent prognosticator.

BCHE is the less intuitive finding in oncology. Known mainly as a serum cholinesterase that hydrolyzes acetylcholine and other choline esters, it also participates in cholinergic signaling, lipid metabolism and inflammation, and changes in cholinergic tone can alter leukocyte trafficking and tumor–stroma crosstalk (44). Low circulating BCHE has long been associated with systemic inflammation, malnutrition and adverse outcomes, and the enzyme is repeatedly identified as a prognostic marker across disease states (45). The most directly relevant evidence comes from head and neck squamous cell carcinoma, where tumor tissue showed markedly dysregulated cholinergic signaling, and high intratumoral BChE activity identified patients with poorer prognosis (46). In our data, BCHE was the single best-supported prognostic OSG: significant in univariate Cox ($P = 0.0094$), retained through LASSO, the only multivariable term retained at $P < 0.1$ ($P = 0.055$), and a significant Kaplan–Meier stratifier with the optimal cutoff ($P = 0.003$; high-versus-low HR = 4.1). It also tracked positively with M0 and M1 macrophages and

resting dendritic cells, which points toward an immunoregulatory dimension rather than a purely cell-autonomous effect. FOXM1 and BCHE were themselves correlated, and their enrichment programs complement each other, cell-cycle proliferation on one side and EMT/Wnt on the other, suggesting convergence on an invasive, microenvironment-responsive malignant state.

The immune findings carry the clearest translational weight. NPC is among the most heavily infiltrated solid tumors and, at the same time, one of the most effective at immune evasion (47). EBV is central to that paradox. Latent viral proteins, including LMP1, reshape the malignant compartment and recruit leukocytes while simultaneously suppressing their function, and the virus uses several routes to evade innate and adaptive immunity (48, 49). Our deconvolution reflected this directly. Naïve and memory B cells and naïve and resting-memory CD4 T cells were depleted, while plasma cells, activated-memory CD4 T cells, activated NK cells, M0 and M1 macrophages, resting dendritic cells and neutrophils expanded, a pattern consistent with chronic antigen exposure, terminal B-cell differentiation and myeloid-supported inflammation. The ten-cell LASSO signature compressed these shifts into a compact discriminator, and the single-cell communication analysis showed malignant cells sending MIF, galectin and CD70 signals that can inhibit adjacent lymphocytes. ROS likely reinforce this state: elevated extracellular and intracellular ROS impair T-cell activation and promote exhaustion in the tumor microenvironment (50), linking the oxidative and immune axes directly. FOXM1 correlated weakly with CD274/PD-L1 and TNFRSF9, so FOXM1-high tumors might be preferentially checkpoint-responsive, but the correlations are small and this remains a prediction to test rather than an established effect.

That prediction is worth making because checkpoint blockade has changed the treatment of recurrent or metastatic NPC. Adding toripalimab or tislelizumab to first-line chemotherapy improved progression-free survival in the JUPITER-02 and RATIONALE-309 trials (51, 52), confirming that the immune compartment in NPC is tractable. If validated, markers such as BCHE and FOXM1 could help identify patients most likely to benefit. Our data do not directly measure treatment response, and they cannot support that claim yet.

The ssGSEA and drug-sensitivity results add further hypotheses, with caveats. pRRophetic values are statistical extrapolations from cell-line panels rather than patient response, and we treat them as candidate leads, not treatment recommendations. The direction of the predictions is nonetheless reassuring: estimated IC50 was lower in NPC for cisplatin, docetaxel and gemcitabine (all adjusted $P < 0.01$), the three backbone drugs of current NPC chemotherapy, which gives the pipeline a degree of face validity even though the estimates remain hypothesis-generating. Concordant up-regulation across three independent bulk cohorts, and enrichment within malignant cells at single-cell level, strengthen the transcript-level findings and localize both signals to the tumor compartment, partly offsetting the limitations of bulk microarrays. Protein-level validation specific to NPC is not available in public atlases and remains an experimental priority.

Several limitations qualify these findings. Everything reported here is retrospective and computational, the normal controls are few and partly non-paired, and only 16 progression events were available for modeling. That event count limits the stability of multivariable estimates and helps explain why FOXM1, despite a significant unadjusted Kaplan–Meier split, was not retained after adjustment. Probe-to-gene collapsing and cross-platform merging can leave residual bias even after ComBat. CIBERSORT and ssGSEA estimate composition rather than count cells directly. The mechanistic links among oxidative stress, FOXM1/BCHE and immunity derive from correlation and enrichment, not causal experiments. No in-house cohort or functional data were available. Prospective cohorts and in vitro and in vivo work are needed before either marker can be used clinically.

5. Conclusions

This integrated, multi-cohort analysis identifies two OS-related markers with complementary value in NPC. BCHE carried the strongest prognostic signal: significant in univariate Cox, the sole LASSO-retained multivariable term, and a significant Kaplan–Meier stratifier ($P = 0.003$; HR = 4.1). FOXM1, a proliferation/E2F/G2M-linked marker enriched in malignant cells, also defined a high-risk subgroup ($P = 0.012$) but was not retained after adjustment. BCHE sat within EMT/Wnt programs and FOXM1 within cell-

cycle programs, both inside a remodeled, checkpoint-rich immune compartment. Together with the ten-cell immune signature and a stage-inclusive nomogram, BCHE is a candidate tool for risk stratification, while FOXM1 offers a mechanistic link to proliferation. Both require experimental and prospective validation.

Ethics Statement

This study used only publicly available, de-identified data from GEO; no new human or animal experiments were performed, and ethical approval was therefore not required.

Consent to Participate declaration

Not applicable

Data Availability

All datasets analyzed are public: GSE12452, GSE53819, GSE64634, GSE102349 and GSE150430 (GEO, https://www.ncbi.nlm.nih.gov/geo/); OSGs from GeneCards; immune signatures from MSigDB/LM22; transcription-factor regulons from DoRothEA and ligand–receptor interactions from CellChatDB. Analysis code is provided in the Supplementary Code and is available from the corresponding author on request.

Author Contributions

Z C, D W and B S contributed equally to the work. Conceptualization, methodology, formal analysis and writing—original draft: ZC, BS and DW; writing—review and editing: Y T, CY L, ML Z and C Z; supervision: YT,XDK and CZ. All authors approved the final manuscript.

Funding

This research received no specific funding.

Conflicts of Interest

The authors declare no conflicts of interest.

Acknowledgments

We thank the GEO, GeneCards, MSigDB, DoRothEA and CellChatDB resources for open data.

References

1. Chen YP, Chan ATC, Le QT, Blanchard P, Sun Y, Ma J. Nasopharyngeal carcinoma. Lancet (London, England). 2019;394(10192):64-80.
2. Tang LL, Chen WQ, Xue WQ, He YQ, Zheng RS, Zeng YX, et al. Global trends in incidence and mortality of nasopharyngeal carcinoma. Cancer letters. 2016;374(1):22-30.
3. Young LS, Rickinson AB. Epstein-Barr virus: 40 years on. Nature reviews Cancer. 2004;4(10):757-68.
4. Al-Sarraf M, LeBlanc M, Giri PG, Fu KK, Cooper J, Vuong T, et al. Chemoradiotherapy versus radiotherapy in patients with advanced nasopharyngeal cancer: phase III randomized Intergroup study 0099. Journal of clinical oncology : official journal of the American Society of Clinical Oncology. 2023;41(24):3965-72.
5. Sies H, Jones DP. Reactive oxygen species (ROS) as pleiotropic physiological signalling agents. Nature reviews Molecular cell biology. 2020;21(7):363-83.
6. Moloney JN, Cotter TG. ROS signalling in the biology of cancer. Seminars in cell & developmental biology. 2018;80:50-64.
7. Cheung EC, Vousden KH. The role of ROS in tumour development and progression. Nature reviews Cancer. 2022;22(5):280-97.
8. Clough E, Barrett T, Wilhite SE, Ledoux P, Evangelista C, Kim IF, et al. NCBI GEO: archive for gene expression and epigenomics data sets: 23-year update. Nucleic Acids Res. 2024;52(D1):D138-d44.
9. Stelzer G, Rosen N, Plaschkes I, Zimmerman S, Twik M, Fishilevich S, et al. The GeneCards Suite: From Gene Data Mining to Disease Genome Sequence Analyses. Current protocols in bioinformatics. 2016;54:1.30.1-1..3.
10. Ritchie ME, Phipson B, Wu D, Hu Y, Law CW, Shi W, et al. limma powers differential expression analyses for RNA-sequencing and microarray studies. Nucleic Acids Res. 2015;43(7):e47.
11. Kolde R, Laur S, Adler P, Vilo J. Robust rank aggregation for gene list integration and meta-analysis. Bioinformatics. 2012;28(4):573-80.
12. Johnson WE, Li C, Rabinovic A. Adjusting batch effects in microarray expression data using empirical Bayes methods. Biostatistics. 2007;8(1):118-27.
13. Leek JT, Johnson WE, Parker HS, Jaffe AE, Storey JD. The sva package for removing batch effects and other unwanted variation in high-throughput experiments. Bioinformatics. 2012;28(6):882-3.
14. Aleksander SA, Balhoff J, Carbon S, Cherry JM, Drabkin HJ, Ebert D, et al. The Gene Ontology knowledgebase in 2023. Genetics. 2023;224(1).
15. Kanehisa M, Furumichi M, Tanabe M, Sato Y, Morishima K. KEGG: new perspectives on genomes, pathways, diseases and drugs. Nucleic Acids Res. 2017;45(D1):D353-d61.
16. Yu G, Wang LG, Han Y, He QY. clusterProfiler: an R package for comparing biological themes among gene clusters. Omics. 2012;16(5):284-7.

17. Guo Y, Li L, Zheng K, Du J, Nie J, Wang Z, et al. Development and validation of a survival prediction model for patients with advanced non-small cell lung cancer based on LASSO regression. Frontiers in immunology. 2024;15:1431150.
18. Blanche P, Dartigues JF, Jacqmin-Gadda H. Estimating and comparing time-dependent areas under receiver operating characteristic curves for censored event times with competing risks. Statistics in medicine. 2013;32(30):5381-97.
19. Pajouheshnia R, Pestman WR, Teerenstra S, Groenwold RH. A computational approach to compare regression modelling strategies in prediction research. BMC Med Res Methodol. 2016;16(1):107.
20. Subramanian A, Tamayo P, Mootha VK, Mukherjee S, Ebert BL, Gillette MA, et al. Gene set enrichment analysis: a knowledge-based approach for interpreting genome-wide expression profiles. Proceedings of the National Academy of Sciences of the United States of America. 2005;102(43):15545-50.
21. Liberzon A, Birger C, Thorvaldsdóttir H, Ghandi M, Mesirov JP, Tamayo P. The Molecular Signatures Database (MSigDB) hallmark gene set collection. Cell Syst. 2015;1(6):417-25.
22. Newman AM, Liu CL, Green MR, Gentles AJ, Feng W, Xu Y, et al. Robust enumeration of cell subsets from tissue expression profiles. Nat Methods. 2015;12(5):453-7.
23. Hänzelmann S, Castelo R, Guinney J. GSVA: gene set variation analysis for microarray and RNA-seq data. BMC Bioinformatics. 2013;14:7.
24. Geeleher P, Cox N, Huang RS. pRRophetic: an R package for prediction of clinical chemotherapeutic response from tumor gene expression levels. PLoS One. 2014;9(9):e107468.
25. Garnett MJ, Edelman EJ, Heidorn SJ, Greenman CD, Dastur A, Lau KW, et al. Systematic identification of genomic markers of drug sensitivity in cancer cells. Nature. 2012;483(7391):570-5.
26. Hao Y, Stuart T, Kowalski MH, Choudhary S, Hoffman P, Hartman A, et al. Dictionary learning for integrative, multimodal and scalable single-cell analysis. Nat Biotechnol. 2024;42(2):293-304.
27. Osorio D, Zhong Y, Li G, Xu Q, Yang Y, Tian Y, et al. scTenifoldKnk: An efficient virtual knockout tool for gene function predictions via single-cell gene regulatory network perturbation. Patterns (New York, NY). 2022;3(3):100434.
28. Garcia-Alonso L, Holland CH, Ibrahim MM, Turei D, Saez-Rodriguez J. Benchmark and integration of resources for the estimation of human transcription factor activities. Genome Res. 2019;29(8):1363-75.
29. Aibar S, González-Blas CB, Moerman T, Huynh-Thu VA, Imrichova H, Hulselmans G, et al. SCENIC: single-cell regulatory network inference and clustering. Nat Methods. 2017;14(11):1083-6.
30. Qiu X, Mao Q, Tang Y, Wang L, Chawla R, Pliner HA, et al. Reversed graph embedding resolves complex single-cell trajectories. Nat Methods. 2017;14(10):979-82.
31. Jin S, Guerrero-Juarez CF, Zhang L, Chang I, Ramos R, Kuan CH, et al. Inference and analysis of cell-cell communication using CellChat. Nat Commun. 2021;12(1):1088.

32. Gustavsson EK, Zhang D, Reynolds RH, Garcia-Ruiz S, Ryten M. ggtranscript: an R package for the visualization and interpretation of transcript isoforms using ggplot2. Bioinformatics. 2022;38(15):3844-6.
33. Youness RA, Elemam NM, Abdelhamid AM, Mohamed AH, Elsherbiny LM, Ramzy A, et al. Macrophage migration inhibitory factor (MIF) and the tumor ecosystem: a tale of inflammation, immune escape, and tumor growth. Frontiers in immunology. 2025;16:1636839.
34. Noe JT, Mitchell RA. MIF-Dependent Control of Tumor Immunity. Frontiers in immunology. 2020;11:609948.
35. Klibi J, Niki T, Riedel A, Pioche-Durieu C, Souquere S, Rubinstein E, et al. Blood diffusion and Th1-suppressive effects of galectin-9-containing exosomes released by Epstein-Barr virus-infected nasopharyngeal carcinoma cells. Blood. 2009;113(9):1957-66.
36. Lefebvre A, Trioën C, Renaud S, Laine W, Hennart B, Bouchez C, et al. Extracellular vesicles derived from nasopharyngeal carcinoma induce the emergence of mature regulatory dendritic cells using a galectin-9 dependent mechanism. Journal of extracellular vesicles. 2023;12(12):e12390.
37. Flieswasser T, Van den Eynde A, Van Audenaerde J, De Waele J, Lardon F, Riether C, et al. The CD70-CD27 axis in oncology: the new kids on the block. Journal of experimental & clinical cancer research : CR. 2022;41(1):12.
38. Halasi M, Gartel AL. Targeting FOXM1 in cancer. Biochemical pharmacology. 2013;85(5):644-52.
39. Park HJ, Carr JR, Wang Z, Nogueira V, Hay N, Tyner AL, et al. FoxM1, a critical regulator of oxidative stress during oncogenesis. The EMBO journal. 2009;28(19):2908-18.
40. Luo W, Gao F, Li S, Liu L. FoxM1 Promotes Cell Proliferation, Invasion, and Stem Cell Properties in Nasopharyngeal Carcinoma. Front Oncol. 2018;8:483.
41. Yu C, Chen H, Zhao Y, Zhang Y. Forkhead Box Protein M1 Promotes Nasopharyngeal Carcinoma Cell Tumorigenesis Possibly via the Wnt/β-Catenin Signaling Pathway. Medical science monitor : international medical journal of experimental and clinical research. 2021;27:e931970.
42. Li D, Ye L, Lei Y, Wan J, Chen H. Downregulation of FoxM1 sensitizes nasopharyngeal carcinoma cells to cisplatin via inhibition of MRN-ATM-mediated DNA repair. BMB reports. 2019;52(3):208-13.
43. Huang PY, Li Y, Luo DH, Hou X, Zeng TT, Li MQ, et al. Expression of Aurora-B and FOXM1 predict poor survival in patients with nasopharyngeal carcinoma. Strahlentherapie und Onkologie : Organ der Deutschen Rontgengesellschaft [et al]. 2015;191(8):649-55.
44. Hajimohammadi S, Lockridge O, Masson P. New views on physiological functions and regulation of butyrylcholinesterase and potential therapeutic interventions. Frontiers in molecular biosciences. 2025;12:1625318.
45. Santarpia L, Grandone I, Contaldo F, Pasanisi F. Butyrylcholinesterase as a prognostic marker: a review of the literature. Journal of cachexia, sarcopenia and muscle. 2013;4(1):31-9.
46. Castillo-González AC, Nieto-Cerón S, Pelegrín-Hernández JP, Montenegro MF, Noguera JA, López-Moreno MF, et al. Dysregulated cholinergic network as a novel

biomarker of poor prognostic in patients with head and neck squamous cell carcinoma. BMC cancer. 2015;15:385.
47. Jiang J, Ying H. Revealing the crosstalk between nasopharyngeal carcinoma and immune cells in the tumor microenvironment. Journal of experimental & clinical cancer research : CR. 2022;41(1):244.
48. Zheng X, Huang Y, Li K, Luo R, Cai M, Yun J. Immunosuppressive Tumor Microenvironment and Immunotherapy of Epstein-Barr Virus-Associated Malignancies. Viruses. 2022;14(5).
49. Lo AK, Dawson CW, Lung HL, Wong KL, Young LS. The Role of EBV-Encoded LMP1 in the NPC Tumor Microenvironment: From Function to Therapy. Front Oncol. 2021;11:640207.
50. Chen X, Song M, Zhang B, Zhang Y. Reactive Oxygen Species Regulate T Cell Immune Response in the Tumor Microenvironment. Oxidative medicine and cellular longevity. 2016;2016:1580967.
51. Mai HQ, Chen QY, Chen D, Hu C, Yang K, Wen J, et al. Toripalimab Plus Chemotherapy for Recurrent or Metastatic Nasopharyngeal Carcinoma: The JUPITER-02 Randomized Clinical Trial. Jama. 2023;330(20):1961-70.
52. Yang Y, Pan J, Wang H, Zhao Y, Qu S, Chen N, et al. Tislelizumab plus chemotherapy as first-line treatment for recurrent or metastatic nasopharyngeal cancer: A multicenter phase 3 trial (RATIONALE-309). Cancer cell. 2023;41(6):1061-72.e4.